ALUMINA-ALUMINUM TITANATE-TITANIA NANOCOMPOSITE: SYNTHESIS, SINTERING STUDIES, ASSESSMENT OF BIOACTIVITY AND ITS MECHANICAL AND ELECTRICAL PROPERTIES

by

VIKAS SOMANI
Bachelor of Technology, Indian Institute of Technology, 2004

A thesis submitted in partial fulfillment of the requirements
for the degree of Master of Science
in the Department of Mechanical Materials and Aerospace Engineering
in the College of Engineering and Computer Science
at the University of Central Florida
Orlando, Florida

Spring Term
2006

ABSTRACT

This thesis reports the development, synthesis and characterization of a ceramic-ceramic nanocomposite system for its possible application as structural and electronic biomaterial in the biomedical industry. The study selected and synthesized alumina-aluminum titanate-titania (Al_2O_3-Al_2TiO_5-TiO_2) nanoceramic composite using a simple Sol-Gel technique, which can be easily reproduced. Aluminum propoxide and titanium propoxide were used as precursor chemicals. Propanol and 2- methoxy ethanol were used as solvent and stabilizer, respectively. Thermal analyses were performed for a systematic understanding of phase evolution from the synthesized gel. X-Ray diffraction technique was used to confirm the phase evolution, phase purity, crystallite size and crystal structure(s) of the phase(s). Calcination of the powder at low temperatures (700°C) leads to formation of Al_2O_3-TiO_2 nanocomposite and at higher temperatures into Al_2O_3-Al_2TiO_5-TiO_2 nanocomposite confirmed by XRD analysis. Electron microscopic techniques were used to investigate powder morphology, crystallite size and inter-planner spacing. High Resolution Transmission Electron Microscopy images of the calcined powder showed agglomerates of powder particles with particle size in 15-20 nm range.

As-synthesized powder was uniaxially pressed into cylindrical pellets and sintered at elevated temperatures (1000-1400^{o}C) to study the sintering behavior, densification characteristics, and measurement of mechanical and electrical properties and assessment of bioactivity. Phase transformation induced by the sintering process was analyzed by X-ray powder diffraction technique. The effects of nanosize of powder particles and multi-phases on densification, and mechanical and electrical properties were investigated. Vickers hardness and biaxial flexural strength tests were used to determine mechanical properties.

Bioactivity of the nanocomposite was assessed in Simulated Body Fluid (SBF), which has the same ionic concentration as that of human plasma. Effects of biodegradation and change in mechanical properties of the composite when kept in SBF and maintained in a static condition were studied in terms of weight loss, change in the pH of the acellular solution and change in mechanical properties (hardness and biaxial strength). Scanning Electron Microscopy was used to observe the formation of apatite crystals on the surface of the nanocomposite specimens soaked in SBF. The results obtained throw light on biocompatibility and bioactivity of Al_2TiO_5 phase, which has not been reported so far in the literature to the best of our knowledge.

Dielectric constant and dissipation factor of the sintered nanocomposite pellets were measured using HP 4284A impedance-capacitance-resistance meter and 16451 B dielectric test fixture at 1 MHz frequency. The effects of sintering time, temperature and phases present on the electrical properties were studied and are reported in the thesis.

Dedicated to my family and friends.

ACKNOWLEDGMENTS

I take this opportunity to thank Dr. Samar J. Kalita for his support, motivation and fruitful discussions throughout this research work. His systematic approach in research, his constant advice to remain focused and his benevolence made my research and academic study an interesting and rewarding experience. I am very thankful to Dr. Sudipta Seal and Dr. Linan An for serving as my thesis committee members and evaluating this thesis. I would also like to thank Department of Mechanical Materials and Aerospace Engineering, Materials Characterization facility and Advanced Materials Processing and Characterization facility, UCF for their financial and experimental support.

I would like to thank Dr. Helge Heinrich and his student Mr. Ankush Halbe for giving me the opportunity to learn and operate TEM. I am also thankful to Dr Yongho Sohn and his student Mr. Narayana Garimella for DSC/TGA experimental support. Thanks to Dr. Raj Vaidyanathan and Mr. R. Mahadevan Manjeri for low temperature DSC experimental support. I am also thankful to Mr. Kirk Scammon and Mr. Zia Ur Rehman for teaching me XRD and SEM use respectively.

My special thanks to Mr. Himesh Bhatt, Mr. Shipeng Qui, Ms. Abhilasha Bardhwaj, Ms. Faye Tenannbaum and Mr. Vadim Litshovik, my lab and group mates, who helped me in my research work. I had the fortune of staying with three bright and friendly colleagues all from MMAE. I am thankful to all of them Mr. Satyanarayana Kuchibhatala, Mr. R. Mahadevan Manjeri and Mr. Satyajeet Sharma for many invigorating and illuminating discussions. I would

also like to thank all the faculty, students and staff of MMAE for their guidance and support.

My special thanks to many of my friends from Indian Institute of Technology, Roorkee who have been a source of inspiration and help. This research would not have come true without the seeds sown during my primary and undergraduate study and I am grateful to all my teachers who have guided me throughout my studies.

Finally, above all, I am indebted to my parents and my brother for supporting and encouraging me to pursue graduate study.

TABLE OF CONTENTS

LIST OF FIGURES

LIST OF TABLES

LIST OF ACRONYMS/ABBREVIATIONS

THR	Total Hip Replacement
DSC	Differential Scanning Calorimetry
TGA	Thermal Gravimetric Analysis
XRD	X Ray diffraction
SEM	Scanning Electron Microscopy
TEM	Transmission Electron Microscopy
HR-TEM	High Resolution Transmission Electron Microscopy
SBF	Simulated Body Fluid
AT	Aluminum Titanate (Al_2TiO_5)

CHAPTER ONE:

INTRODUCTION

1.1 Motivation

Over 500,000 total hip replacements are performed in the United States each year. 10 percent of the implanted prosthesis requires revision within 10 years, the average life span of an implant is only about 15 years [1]. This short life span creates a problem for the growing number of people receiving implants who are younger than 40 years old. From 1998 to 2001 the number of THR patients less than 40 years of age increased by 8%. The problem is accentuated since younger people are generally more active, and more active patients require multiple revision surgeries in their lifetimes. Figure 1 gives the trend in primary and THR implants up to 2010. Because of the increasing number of hips needed, new materials are needed for THR to improve their durability, and thereby decrease the need for revision surgeries. Similarly, there is an imminent need to develop new and better non-metallic biomaterials for structural bone grafts.

A major driving force in the research and development of new biomaterials and devices is to try to match their performances to that of natural biological systems such as human brain. A promising field in which electronic biomaterials find a wide application is to interface electronics to nerves. Electronic implants have been used in basic research to understand working principles of the brain, to analyze processing of information, to unravel principles of connectivity within the nervous system and to study cell-cell interactions in subsets of neuronal populations[2, 3] .Attempts have been made to implant electrodes concentrated on sensory functions and

simulation of muscles. Materials used for fabricating these electrodes have to be selected after due diligence. The substrate, which carries the electrodes, must be completely insulating to prevent cross-talking between them. The choice of the material also depends on the possibilities and restrictions arising from the fabrication process [2].

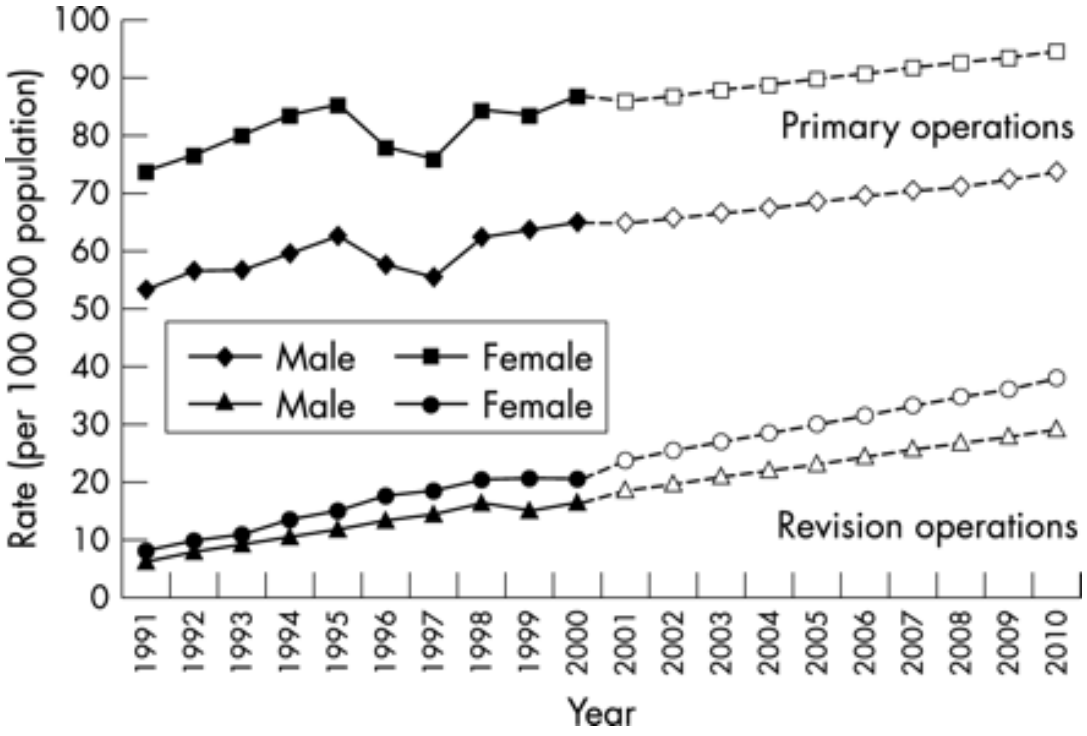

Figure 1. Trends in primary and total hip replacement rates. Source: HES, Department of Health.

There is a need to develop biocompatible electronic materials and devices for *in vivo* diagnostics and implant technologies. It will be of significant biomedical importance if continuous monitoring of performance is made possible for structural implants such as total hip prostheses (THP) using microchips. Today, bioelectronics is a growing interdisciplinary field. Worldwide market for electronic implants was $9.68 billion in 2004, which is growing at the rate

of 14% annually to reach $18.65 billion in 2009. Electronic implants, which release electrical pulses to relieve pain in extreme cases like spinal cord injury, are being researched. It is time to develop biocompatible electronic materials for these applications. But there are few reports of systematic investigations on such multipurpose bioelectronic materials [4, 5].

1.2 Research Objective

The objective of this research was to develop a promising ceramic-ceramic composite system that can fit into multiple purposes *in vivo*. After extensive literature survey and preliminary experimental results this work decided to develop alumina-aluminum titanate-titania nanocomposite for potential applications such as:

1. Structural biomaterial for applications such as femoral head in THR and
2. Bioelectronic dielectric materials for sensor packaging and biochips.

The initial part of study was the synthesis of the ceramic nanocomposites followed by characterization of the composite to evaluate its efficiency for the desired applications. Another aim of this research was to explore the benefits of nanomaterials, which have been shown to possess superior mechanical and electrical properties for use as load bearing biomaterials. The following section elucidates the rationale for choosing the particular composite system and the research plan followed during the study.

1.3 Research Plan

1.3.1 Rationale for choosing Al_2O_3-Al_2TiO_5-TiO_2 nanocomposites and Sol gel synthesis

All materials intended for use in a total hip replacement should have four characteristics in

common:

- Biocompatible; that is, they can function in the body without creating either a local or a systemic rejection response.
- Resistant to corrosion, degradation and wear, so they will retain their strength and shape for a long time. Resistance to wear is particularly significant in maintaining proper joint function and preventing the further destruction of bone due to particulate debris generated as the implant parts move against each other.
- They should have mechanical properties that duplicate the structures they are intended to replace; for example, they are strong enough to take weight-bearing loads, flexible enough to bear stress without breaking and able to move smoothly against each other as required.
- They meet the highest standards of fabrication and quality control at a reasonable cost.

The last few years has seen an increased research in the area of composites for use as femoral heads in total hip replacements. Since friction and wear are of prime importance in choosing materials for total hip replacements, composites are assumed to be superior to ceramics. Composites can be tailored / designed to have constituents which can improve its wear resistance and flexural strength. Among other materials that have been researched alumina and composites of alumina-titania are worth mentioning. Al_2O_3-TiO_2 composites have been characterized for use as femoral head [6]. Metco 131 (60 wt % alumina and 40 wt % Titania) has also been proposed for biomedical application. The initial reports have been encouraging but extensive investigation needs to be conducted before these composites can be used *in vivo* as

femoral head [6].

Based on the literature research and considering the properties of materials suitable for use *in vivo* both as a candidate for load bearing bone graft and as a bioelectronic material I decided to concentrate my efforts on synthesis of Al_2O_3-Al_2TiO_5-TiO_2 nanocomposite.

1.3.2 Al_2O_3-Al_2TiO_5-TiO_2 nanocomposites.

Various materials have been investigated for *in vivo* applications. Alumina is one of the most researched bioceramic because of the following favorable properties [7]:

1. Dimensional stability
2. Chemical inertness
3. Excellent mechanical properties.
4. Absence of any adverse local tissue response.

It is estimated that two million alumina ball heads have been implanted world wide since its first clinical application. Alumina has been shown to possess higher wear resistance than metals.

Alumina has been investigated for use in-vivo for several other applications. Applications such as; ball heads of hip joint prostheses, sockets of hip joint prostheses, socket inlays of hip joint prostheses, femoral or tibial components of knee prostheses, shoulder prostheses and finger prostheses and dental implants are known or have been investigated, although some of them did not achieve high commercial significance [8]. Moreover alumina is known to possess excellent insulating properties with a dielectric constant of 9 and has been studied extensively for replacing SiO_2 in future semiconductor devices.

During the last decades titanium and its alloys have been used successfully in implantology and orthopedics to replace damaged bone. If the tissues can better adhere to the surface of the implant, many clinical problems can be avoided. Sol-gel-derived titania coatings attract calcium and phosphate from the body fluid and form bone-like calcium phosphate, [hydroxyl carbonate apatite (HCA)] on the surface i.e. titania coated implants are bioactive [9].

After deciding on the composite system my next goal was to select a synthesizing process which can provide a simple and repeatable procedure to synthesize the nanocomposite and tailor its composition according to needs.

1.3.3 Sol gel emerges as the process of choice

Though a number of processes have been used to synthesize nanocomposites, sol-gel synthesis was used for synthesizing the nanocomposites in this study. Sol-gel synthesis of materials offers several advantages like: low temperature synthesis, ease in controlling composition variations, low cost and potential use in film processing. Figure 2 is a flowchart which gives a view of the research plan adopted and followed in this study.

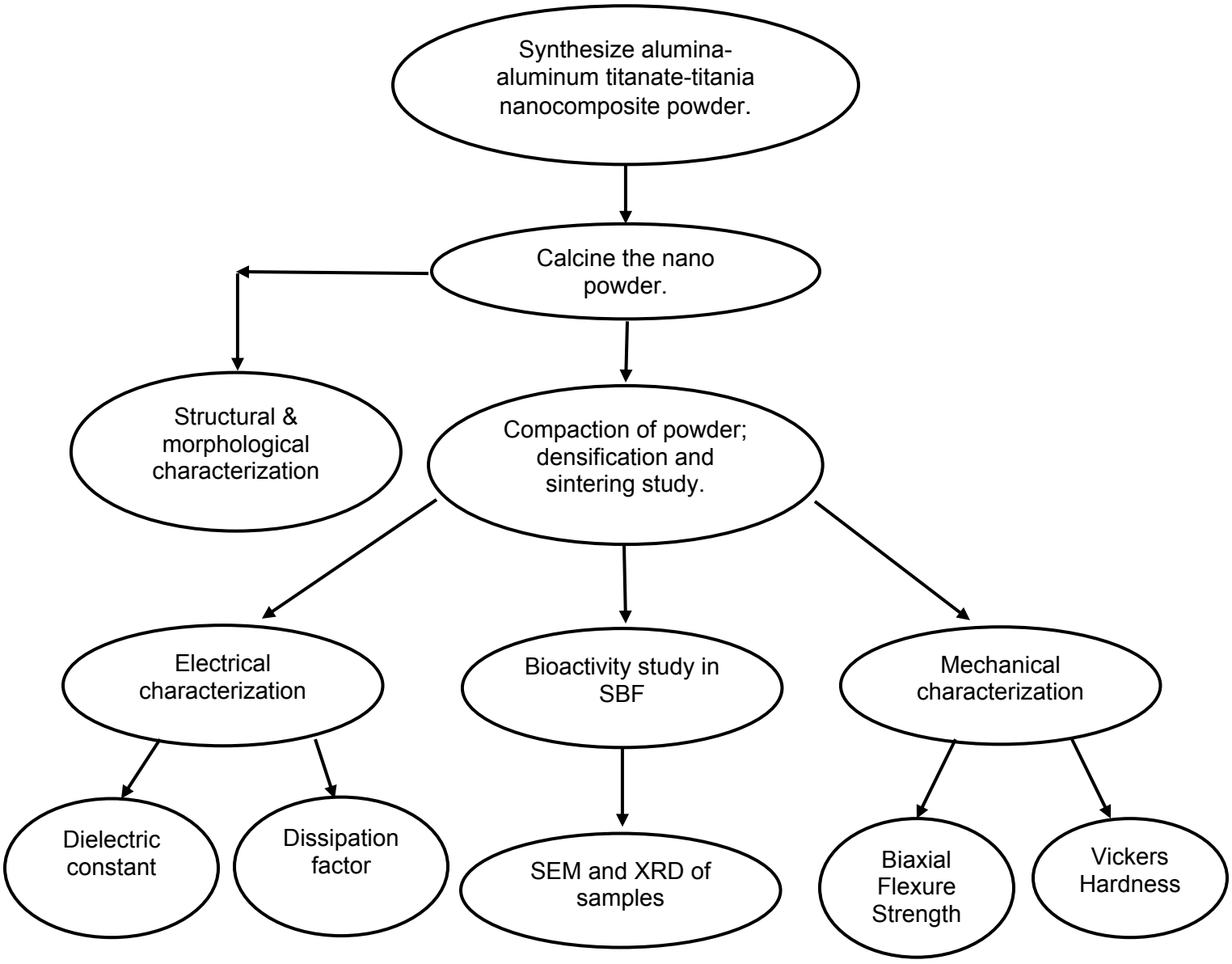

Figure 2. Flowchart of the research plan followed in this study.

CHAPTER TWO:

LITERATURE REVIEW

2.1 Biomaterials

2.1.1 Biomaterials in load bearing applications

Biomaterials have proved to be a boon for patients suffering from musculo-skeletal defects, diseases and/or injuries. Biomaterials are by definition synthetic materials used to make devices to replace part of a living system or to function in contact with living tissue. More than 43 million people have some form of arthritis and this figure is set to increase dramatically to 60 million by 2020. The growing age of baby boomers and the increasing life expectancy means that many people outlive the quality of their connective tissues [10].

Implant insertion into the human body elicits an immediate response from the immune system. Ceramic biomaterials are divided into 3 broad categories based on their interaction with the human tissue:

1. Bioactive ceramic like hydroxyapatite.
2. Bioresorbable ceramic like tricalcium phosphate.
3. Bioinert ceramics like alumina, titania and zirconia.

Bioactive materials (mostly ceramics) undergo chemical reactions at the interface and lead to bonding of tissues at the interface. Bioresorbable implants on the other hand degrade gradually with time and are replaced by natural tissues. Bioinert materials as the name suggests do not

interact with the physiological system and are always treated as foreign materials by the body.

2.2 Total Hip Replacement (THR)

2.2.1 Material properties for in vivo applications as THR

THR are permanent implants unlike those used to treat fractures and the extensive bone and cartilage removed during implantation makes this procedure irreversible. The prosthesis for total hip replacement consists of a femoral component and an acetabular component (Figure 2). The femoral stem is divided into head, back and shaft. Various materials or alloys which have been investigated or used as THR are:

1. 316 L stainless steel, Cobalt-chromium alloys and Titanium alloys for femoral stems.
2. Alumina and zirconia for femoral head.
3. Ultra high molecular weight polyethylene (UHMWPE) as cup.

Ceramics in THR are classified into materials that are either Bioinert (ex- alumina and zirconia) or bioactive (ex- hydroxyapatite and bioglass). Both these classes of ceramics find different application within the THR. Bioinert ceramics are used as femoral head and bioactive ceramics as coating material in the cementless implant [11]. Hip is a dynamic component in the human body. Due to the dynamic nature of the human activity, the cartilage of the hip is exposed to about eight times body weight during fast walking. Over a period of 10 years an active person may subject the cartilage of the hip to more than 17 million weight bearing cycles [12]. Various components of THR must be able to withstand and transmit the cyclically fluctuating forces caused by gravity and muscular action. Therefore properties like strength, toughness, elasticity,

ductility and low friction rates are highly desired. The various systems or combinations used in a THR are [13]:

2.2.2 Metal-on- Polymer Implant.

The metal and polymer implants are the most commonly used hip replacement implants. Both the ball and the socket of the hip joint are replaced with a metal prosthesis, and a polymer spacer is placed in between. The metals used include titanium, stainless steel, and cobalt chrome.

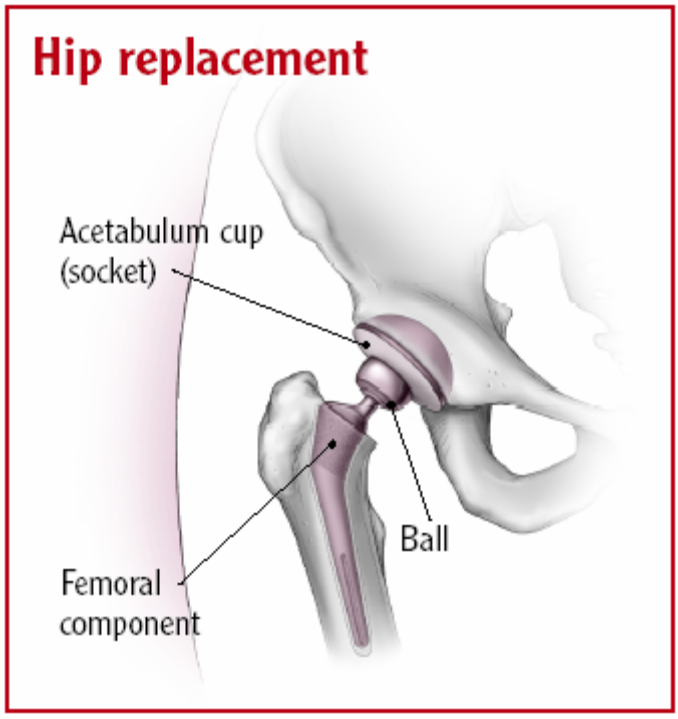

Figure 3. Total Hip Replacement and its various parts.

The implant is secured to the bone by one of two methods; it is either press-fit or cemented into place. In the press-fit method, the implant is fit snuggly into the bone, and new bone forms around the implant to secure it in position. When an implant is cemented, special bone cement is

used to secure the prosthesis in position.

Although the resistance of UHMWPE to friction enhances the biofunctionality of this material, its biocompatibility is questionable. Like metals, UHMWPE is well tolerated in bulk form but harmful when it is degraded. Since it is a polymer, it is subject to oxidation in the body, a process that produces many free radicals, including nitric oxide, hydrogen peroxide, and hydroxide [1].

2.2.3 Metal-on-Metal Implant

Metal-on-metal implants use similar materials, but there is no plastic piece inserted between. Metal-on-metal implants do not wear out as quickly as the metal-on-plastic implants. The metal-on-plastic implants wear at a rate of about 0.1 millimeters each year. Metal-on-metal implants wear at a rate of about 0.01 millimeters each year, about 10 times less than metal and plastic.

Despite the low wear rates, it is not known that metal-on-metal implants will last longer. There are also concerns about the wear debris that is generated from the metal-on-metal implants. Metal ions are released into the blood, and these metal ions can be detected throughout the body. The concentration of these metal ions increases over time. There are no data to show that these metal ions lead to increased rates of cancer or disease, but no one knows for sure.

2.2.4 Ceramic-on-ceramic implant

These are designed to be the most resistant to wear of all available hip replacement

implants. They wear even less than the metal-on-metal implants. Ceramics are more scratch resistant and smoother than any of these other implant materials. Again, there is no long term data available on how well these implants work over time. Also there are concerns that these ceramic implants can break inside the body. There has been fear of a possibility of catastrophic failure in case of ceramic implants. Some other concerns related to these implants are the weight of the patients and the acetabular cup loosening.

2.2.5 Metal and highly cross linked polyethylene

One of the more commonly used implants is new types of polymers that are designed to be more resistant to wearing out. These so-called highly cross linked polymers are manufactured in a way that they wear out less quickly than the traditional polymers. These new implants have only been available for a few years, so whether or not they do work better than traditional plastic implants, we will not know for quite some time.

It is now accepted that the ceramic-on ceramic and metal-on-metal implants are more durable than the conventional implants [14]. The main drawback with ceramic-on-ceramic and metal-on-metal implants is their cost. For example, a ceramic-on-ceramic implant is twice as expensive as a conventional metal-on-plastic implant. So the conservative approach has been to reserve the longer lasting, more expensive implants for younger and more active patients and use the conventional design for older and less active people. But with increasing average life expectancy due to improving health facilities the line between young and old these days is growing fainter. At age 65, an American woman now has, on average, another 19 years ahead of her, and an American man, another 16 years. Many older people are quite active. All of these

factors have to be considered. Certainly age alone can't be used to decide which type of hip replacement is right for someone.

2.3 Need for nanomaterials for biomedical applications.

Nanomaterials are considered as a new class of material as they possess superior properties over their microscale counterparts. The longevity of THRs is a major research field and efforts to improve its performance have been focused on better design, fabrication and material property requirements [15]. Efforts to increase the durability of artificial hip joints have focused mainly on reducing the quantity of wear generated at the implant bearing surfaces. Improvements in the quality of the metal-on-UHMPE articulation have contributed to reduced wear. However, ceramic-on-ceramic bearing surfaces such as alumina-on-alumina have demonstrated some of the lowest wear rates reported in literature and have emerged as a possible solution to the wear related problems of the earlier components. These ceramic implants normally possess grain sizes on the scale of micrometers. Particulate wear generated from alumina-on-alumina bearing surfaces could be further reduced significantly if ultrafine or nanosized grains were present at the bearing surface.

The drive towards the use of ultrafine-grained materials and nanomaterials is due mainly to the improvements in mechanical and wear properties they can offer [16]. The mechanical properties of nanoceramics such as hardness and strength are generally superior to those of conventional ceramics. It is well known that the wear characteristics of conventional ceramics can be improved by reducing grain size, and even more so by the use of ceramics with nanosized grains. For these reasons, the study of these ceramics for bearing application is of high relevance

and importance. One of the main impediments to the use of nanopowders is their higher cost compared to conventional ceramic powders, and the retainment of the nanostructure in the final product after exposure to elevated temperatures during processing.

2.3.1 Need for nanocomposites for bone grafting

Single-phase materials do not always provide all the properties necessary for implants and sometimes are very far from the characteristics of a true implant. Nanocomposites could play a pivotal role in fabrication of implants as a new class of material, which may use a combination of several nanoscale materials and/or in conjunction with osteoinductive growth factors and osteogenic cellular components. The term nanocomposite can be defined as a heterogeneous combination of two or more materials in which at least one of the materials should be on a nanometer-scale [17]. Since bone is a typical example of a nanocomposite, designing implants in the form of nanocomposite is perceived to be beneficial over monolithic and microcomposite materials [18].

Bone, a connective tissue, is itself a composite which consists of a polymeric base (collagen), a ceramic phase (mineral hydroxyapatite) and water. It is a porous material which is made of a strong outer covering (cortical shell) and a soft inner region (cancellous bone). It contains voids of varying sizes. Various materials have been developed for use as *in vivo* including metals, ceramics, composites and polymers. Though significant achievements have been made in the last two decades, researchers still need to fabricate a biomaterial which can truly mimic the required functions and properties of human bone (Table 1). It is not an overstatement to say that it is more challenging to develop a biomaterial as biological properties

come into play that are very complex in nature.

Biocomposites are being developed to eliminate the problem of elastic modulus mismatch and stress shielding of bone. There can be two approaches to attack this problem. Bioinert composites, such as carbon–carbon fiber composite materials, are routinely used in aerospace and automotive applications. But the carbon fibres give rise to a chronic inflammatory response. Thus, bioinert composites are not widely used and are unlikely to be a fruitful direction for development.

Table 1: Properties of human bone

Properties	**Measurements**	
	Cortical bone	**Cancellous bone**
Young's modulus (MPa)	14-20	0.05-0.5
Tensile strength (MPa)	50-150	10-20
Compressive strength (MPa)	170-193	7-10
Fracture toughness (MPa $m^{1/2}$)	2-12	0.1
Strain to failure	1-3	5-7
Density (g/cm^3)	1.8-2.2	0.1-1.0
Apparent density (g/cm^3)	1.8-2.0	0.1-1.0

The second approach is to make a bioactive composite that does not degrade. The result is a material that has an elastic modulus that is much closer to that of bone and will produce a bioactive bond to bone when implanted. An important advantage of this concept is that the

mechanical properties of strength and elastic modulus can be controlled, within limits, by varying the volume fraction, size and distribution of the second phase. Ideally, it is possible to match the properties of both cancellous and cortical bone, although, this is seldom achieved by the biocomposites available today. A challenge for the next decade is to use advanced materials processing technology to improve the interfacial bonding between the phases and thereby increase strength and fracture toughness of these new materials [19].

My aim was to make a material with properties equivalent to the femoral head by integrating all the factors associated with osteoconduction, osteoinduction, and osteogenicity. Using the composite approach, it is possible to manipulate the mechanical properties such as strength and modulus of the composites close to the requirements with help of secondary substitution phases. For example, HA-polymer composites have an elastic modulus near to that of bone and are more mechanically reliable than their monolithic constituents [17].

2.4 Bioelectronic materials

Bioelectronics is a progressing interdisciplinary research field that involves the integration of biomaterials with electronic transducers, such as electrodes, field-effect-transistors or piezoelectric crystals. An example of a bioelectronic device is a microelectrode probe fabricated from silicon using microfabrication techniques from semiconductor industry [20]. Since the microprobe is used *in vivo* the materials used for its fabrication must be biocompatible. One way to circumvent this problem is to encapsulate the entire device in a biocompatible material and allow only the sensory parts to be in touch with biological fluids/tissues. But this is only a temporary solution since any leakage or defect in the encapsulating biocoating can have drastic consequences for the surrounding tissues. This problem gets accentuated if the device is required

to work for a long time *in vivo*.

MEMS technology for application in biosensors and the adaptation of various types of sensors to *in vivo* diagnostics has seen an upsurge in activity in the last few years. Figure 3 shows a schematic of a biomolecular sensor developed for *in vivo* application. This is due in part to the formidable challenges faced in the more general field of implantable biosensors [21]. Long-term *in vivo* sensing is a critical component of the ideal closed-loop drug delivery or monitoring system, but the issue of implant biocompatibility and biofouling must be addressed in order to achieve long-term *in vivo* sensing

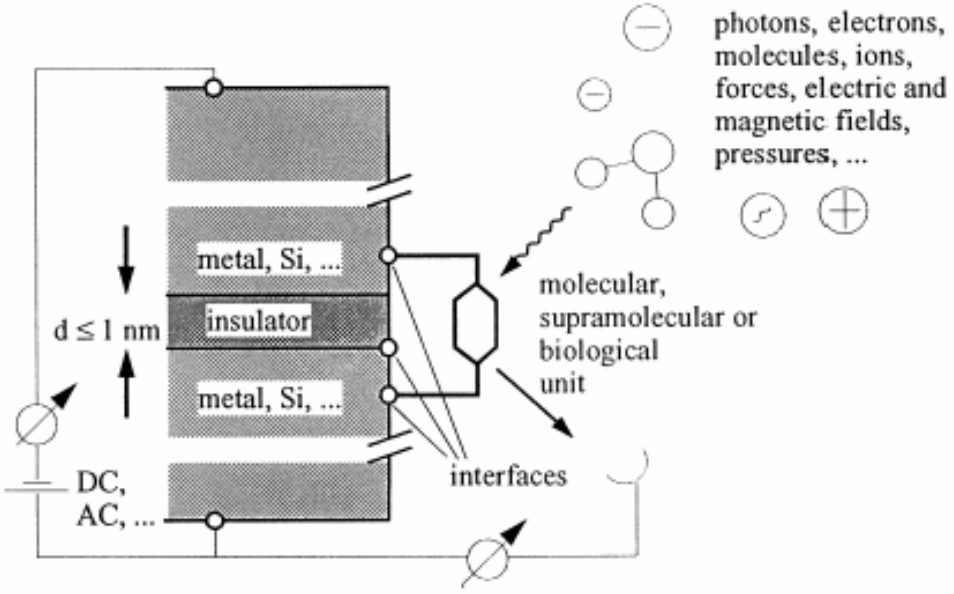

Figure 4. Schematic of a (bio)molecular sensor device showing coupling between microelectronic structures and chemically synthesized or biological structures.

Although it is important to avoid adverse tissue responses to any implant, the degree of biocompatibility must be greater for a sensor. Even those materials generally considered to be biocompatible produce some degree of tissue response, usually resulting in the partial isolation of the implant from the body. Although this typically does not impede the function of drug

delivery, orthopedic, or other implants whose function is essentially mechanical in nature, implant isolation leads to reduced sensitivity and increased delay time for a sensor.

Microfabricated pressure sensors also have the potential for *in vivo* application. A capacitance-based pressure sensor can be microfabricated with a membrane that deforms according to pressure difference, causing a change in capacitance between the membrane and an electrode on the surface of the device. These systems could be implanted in small mammals to measure blood pressure during studies of hypertension and cardiovascular physiology. Another capacitance based pressure sensor has been fabricated for intraocular implantation in glaucoma patients [22].

2.4.1 Biocompatibility issues related to electronic materials

The biocompatibility of electronic materials was not addressed until recently because these materials were packaged or encapsulated away from direct contact with tissue and fluids; biocompatibility is a surface-mediated property, and the biocompatibility of a device depends only on those materials in contact with tissue. The biocompatibility of silicon and other electronic materials has become much more important with the advent of implantable electronic devices that interact directly with the body. The biocompatibility of some MEMS electrode materials has been studied, however, because of their use in other devices such as pacemaker electrodes and dental implants [21].

Conflicting reports have appeared in literature regarding the biocompatibity of materials used in electronic applications *in vivo*. A comprehensive evaluation of silicon materials was

completed by Kotzar *et al.*, who performed the baseline ISO 10 993 tests on single crystal silicon, polycrystalline silicon, silicon dioxide, silicon nitride, single-crystal silicon carbide, titanium, and the photo epoxy SU-8 [23]. They found that only silicon nitride and SU-8 leached detectable nonvolatile residues in aqueous physiochemical tests, and only SU-8 leached detectable nonvolatile residues in isopropyl alcohol. None of the materials were found to be cytotoxic *in vitro* using mouse fibroblast. Another report by Voskerician *et. al.* on biocompatibity of materials like silicon nitride, silicon dioxide, SU-8™ and silicon concluded that though silicon and SU-8™ show no signs of biofouling silicon nitride and silicon dioxide show some biofouling [24].

2.5 Al_2O_3-$AlTiO_5$-TiO_2 Nanocomposites

Our hypothesis in selecting Al_2O_3-$AlTiO_5$-TiO_2 nanocomposites was based on extensive literature survey. The main emphasis was to synthesize and characterize a nanocomposite which can serve dual purpose of:

1. Structural biomaterial for THR and other load bearing applications.
2. Dielectric material for use in future bioelectronics.

A material with these properties would be of immense importance for use in bone implants as well as BIOMEMS implants.

2.5.1 Al_2O_3 and its properties

Al_2O_3, an oxide of aluminum a group III element, is known to be a very stable and robust material. Al_2O_3 (corumdum) has a hexagonal structure and figure 4 shows a schematic of a unit cell of alumina. The use of alumina ceramics in prosthetics and dental implants is based on the

resistance to corrosion of alumina [25]. This results in alumina being bioinert which is most important in medical applications [26]. The material's hardness is extremely high resulting in its low wear. This property is particularly significant when we consider ball heads of hip joint prostheses. The elasticity modulus of alumina is 400 GPa in comparison to 316L stainless steel with 200 GPa and Ti_6Al_4V with 110 GPa. As a result, alumina provides for rigid and non-deformable implants to be produced for use in prosthetics and dental implants.

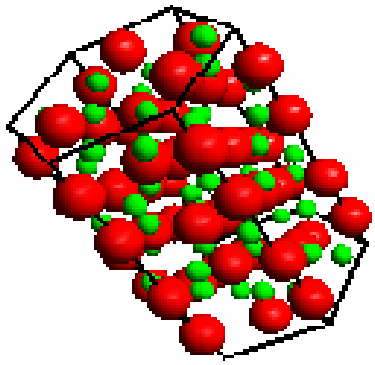

Figure 5. The unit cell for alumina containing aluminium atoms (red) and oxygen atoms (green).

Alumina has high mechanical strength. Dental implants and prosthetic implants alike are always designed as load-accepting implants. The implants remain in the body over a long period of time (i.e. for many years), and therefore must not be susceptible to possible reductions in strength, which could affect their load-carrying function. The high resistance to compression of alumina is very important. Especially in prosthetics, e.g. in hip joint prostheses, high loads must be accepted over long periods of time as such the prosthetic components must not be susceptible to elastic or plastic deformations, since such deformations would cause the wear of the prosthetic components to increase. Important properties of medical-grade alumina are its high corrosion resistance, high Young's modulus, high mechanical strength, bioinertness, high wear resistance, and stiffness.

It has many favorable electrical properties; it has a high band gap, a high electrical breakdown voltage and is thermodynamically stable when in contact with silicon at high temperatures. It shows excellent optical properties and has high transparency down to 250 nm levels [27]. Shamala *et. al.* deposited amorphous alumina thin films by spray pyrolysis process on silicon substrates. The peak dielectric constant of the film was 9.6. Turunen *et. al.* deposited alumina films by high fuel oxy spray technique [28]. The dielectric constant of the film varied from 5.9 to 8.2 over a frequency range of 20 kHz to 1 MHz. Low dielectric constant values were reported for alumina films deposited using lower deposition rates because films deposited using low deposition rates have more interfaces than those deposited using high deposition rates. Hence an important conclusion of this work was that the number of interfaces in dielectric materials play an important role in determining the overall dielectric properties. Katiyar *et. al.* used pulsed laser deposition technique to deposit thin amorphous alumina films on p-type silicon substrates [29].

2.5.2 TiO_2 and its properties

Three polymorphs of TiO_2 (titania) occur in nature: Rutile (tetragonal, space group P42/mmm), Anatase (tetragonal, space group I41/amd) and Brookite (orthorhombic, space Pbca). Rutile is the only stable phase, whereas anatase and brookite are metastable at all temperatures, transforming to rutile when they are heated. Figure 5 shows a schematic of a unit cell of rutile TiO_2. However, anatase is typically the majority product of inorganic syntheses and is the main constituent of nanocrystalline materials. It has been reported that titania normally undergoes anatase - rutile phase transformation in the temperature range from 600 to 700^oC [30]. Smaller

particle size and large surface area have been suggested to favor the transformation, which occurs via nucleation and growth.

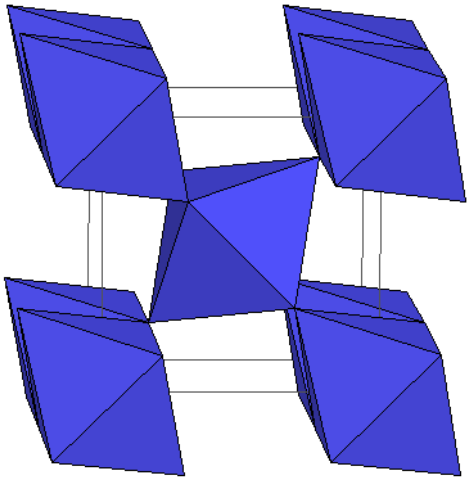

Figure 6. Unit cell of rutile TiO_2.

Ye *et. al.* synthesized titania nanostructured films and bulk specimens with particle size of 8.5 nm using plasma enhanced physical vapor deposition techniques. The nanostructured films showed a dielectric constant which was 10-100 times higher than their coarse grain counterparts. Biocompatibility of titania gels synthesized by chemical routes have been studied by Uchida *et. al.* They concluded that anatase titania because of its crystal structure is conducive for growth of apatite crystals *in vivo*. But other form of titania like rutile phase is not conducive for the growth of apatite [31].

2.5.3 Aluminum titanate (Al_2TiO_5) and its properties

Al_2TiO_5, Aluminum Titanate (AT), a compound of Al_2O_3 and TiO_2 is known to have excellent thermal shock resistance, low thermal expansion coefficient (0.2×10^{-6} to 1.0×10^{-6})

and high melting point [32]. Figure 6 shows the phase diagram of Al_2O_3 and TiO_2. However Al_2TiO_5 undergoes decomposition into Al_2O_3 and TiO_2 in the temperature at 1280°C which limits its applications [33]. The low thermal expansion coefficient is due to the expansion anisopropy of the individual orthorhombic aluminum titanate crystals which results in a stable microcracked structure. Above 1280°C an additive reaction takes place in an oxidizing atmosphere resulting in the formation of aluminum titanate:

$$\alpha\text{-}Al_2O_3 + TiO_2\,(\text{rutile}) = \beta\text{-}Al_2TiO_5$$

β-Al_2TiO_5 has a pseudobrookite crystal structure. The molar free energy of Al2TiOS formation can be estimated by a third-law treatment of the available heat capacity data and the equilibrium temperature and it has been confirmed experimentally:

$$\Delta G^{o}_{\ Al2TiO5} = \Delta H^{o} - \Delta S^{o}T$$

$$= 17000 - 10.95T$$

$$= -10.95\Delta T\ (\text{J/mol})$$

where $\Delta T = T$ - 1553 (K).

Aluminum titanate has an orthorhombic lattice with a *Cmcm* space group, with the following lattice constants: a = 0.3591 nm, b = 0.9429 nm, and c = 0.9636 nm.

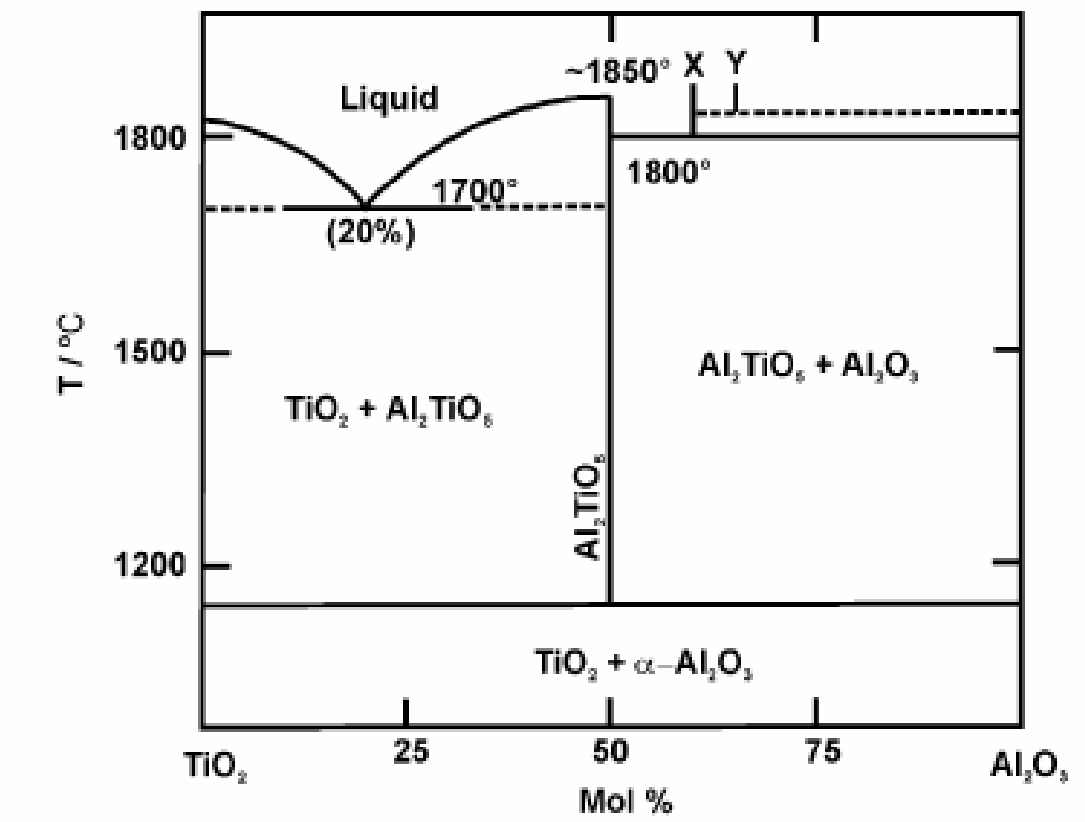

Figure 7. Phase diagram of Al_2O_3-TiO_2 system as proposed by Hoffman *et al*.

2.5.4 Other potential applications of Al_2O_3-$AlTiO_5$-TiO_2 nanocomposites.

SiO_2, with a dielectric constant (κ) of 3.9 in amorphous form, is the ubiquitous dielectric. It has excellent dielectric properties, a high resistivity of 10^{18}`Ω cm and a large band gap of ~ 9 eV. Furthermore SiO_2 forms a very stable interface layer on silicon substrate and is very easy in process integration. But continued miniaturization has put physical limits to the use of SiO_2 as it shrinks to dimensions where quantum mechanical effects become dominant resulting in high leakage current. This has spurred the need to find new dielectrics and a number of reports in the last few years have been based on potential dielectric materials like HfO_2, Al_2O_3, ZrO_2, Ta_2O_5, TiO_2, $BaTiO_3$ and SiN. The dielectric constants of these materials range from $\kappa < 10$ to $\kappa >$

10000.

2.6 Alternate dielectric materials

Since a thinner dielectric thickness between a capacitor means a higher capacitance, the first and easiest way to increase the charge storage capacity is to decrease the thickness of dielectric (silicon dioxide in most cases). But a thinner dielectric layer means a less effective barrier to the movement of charge carriers. This results in a higher dielectric leakage current due to quantum effects of tunneling [34]. An alternate way to increase the capacitance is to use a dielectric with a higher dielectric constant. The increase in dielectric circumvents the problem of increased leakage current as it allows for the use of a thicker dielectric film between the capacitor plates.

2.6.1 Need for nanocomposite dielectrics

The inability and challenges with oxide dielectrics and their compatibility with underlying silicon substrate has led researchers to materials like oxynitrides and oxide/nitride stacks. Table 3 lists some dielectric materials that have been investigated over the last decade and their properties. Silicon oxynitride has a higher dielectric constant, show lower leakage current and has a stable interface with silicon substrate [35]. Though the results are encouraging scaling with oxynitrides seem to be limited to a few years because of their relatively low dielectric constant. Hence more innovative and novel ideas need to be implemented to find a dielectric with the desired properties for future use. It is often possible to form binary alloys and/or composites that have the advantages of the desirable properties from two different oxides while eliminating the undesirable properties.

Table 2. Some dielectric materials and their properties

Material	Dielectric constant	Band Gap (eV)	Crystal structure
SiO_2	3.9	8.9	Amorphous
Si_3N_4	7	5.7	Amorphous
Al_2O_3	9	8.7	Amorphous
Y_2O_3	15	5.6	Cubic
ZrO_2	25	5.8	Mono, tetra, cubic
HfO_2	25	5.7	Mono, tetra, cubic
La_2O_3	30	4.3	Hexagonal, cubic
TiO_2	80	3.5	Tetragonal

Mono: monoclinic, Tetra: tetragonal

2.6.2 Some nanocomposites and their electrical properties

The last decade has seen a phenomenal amount of research going in characterizing nanoscale particles for their physical, mechanical, optical and electronic properties. Ceramics used in electronics are usually called electroceramics and find applications in a wide array of fields. Electroceramics find applications in capacitors, transistors, memory storage operations, sensors and actuators. A significant amount of research has been concentrated on developing models to understand the effect of nanosize on the electronic properties like dielectric property, resistivity and existence of dipoles.

The nanometer length scales in nanostructured materials leads to what is termed as

quantum confinement. The small length scales directly influence the energy band structure and can indirectly lead to changes in the atomic structure. According to basic quantum physics the energies of the electronic states depend on $1/L^2$ where L is the dimension of the system in that particular direction. The gap between two successive energy levels varies inversely to the square of the dimension of the system (L). Thus if the length scale of the system is significantly smaller than the bulk materials the electronic states configuration can be quite different. This results in narrower energy bands eliciting the classical 'particle in a box' like behavior response from the electrons. The result of these changes in the electronic structure is a change in the total energy, if we ignore the entropy considerations, which has important implication on the thermodynamic stability of the system. This may lead to nanomaterials with a different atomic structure than their bulk counterparts [36]. Reduced size can also alter the properties which are otherwise dependent on the electronic energy level arrangements. Properties such as electrical, thermal, optical and magnetic characteristics may also change. Since a number of excellent reviews [37]on electroceramics are available this section will mainly concentrate on the nanoceramic composites and their electrical properties.

The electrical properties of a number of nanocomposites have been investigated in the last few years. These composite systems can be categorized broadly as, Metal-metal nanocomposites, Metal-oxide nanocomposites, Oxide-oxide nanocomposites, Metal-polymer nanocomposites, Oxide-polymer nanocomposites. This section will focus on the first three kinds of nanocomposites.

Tepper *et. al.* [38] studied the SiO_2-W nanocomposites and found that the dielectric

properties were significantly different (higher) from that of pure nano SiO_2. For example, at a frequency of 1 kHz, the dielectric constant of a green compact made of pure silica under the same conditions is about 13 compared to about 30 (below the percolation threshold) and about 3000 (above this threshold) of the nanocomposites. The increase in the dielectric constant was attributed to the interface between the W and SiO_2 particles. The nature of interaction and bonds at these interfaces alter the electrical properties of nanocomposites. In another paper Tepper et. al discuss their findings on electrical properties of pure nanoscale silica [39]. The dielectric constant of amorphous SiO_2 powder with nanometer size particles was higher compared to amorphous SiO_2 thin films. This enhancement was attributed to higher density of Si dangling bonds [40]. The nanosized Al powder was vapor deposited and exposed to air. Due to the high reactivity of nanopowders it formed a thin layer of alumina on its surface. The results suggested the importance of density and consolidation pressure on the electrical properties of nanocomposites. An increase in consolidation pressure and increase in grain size resulted in conducting behavior for most nanocomposites with grain size ranging from 114 nm to 410 nm.

Gao *et. al.* fabricated nanocomposites of TiN-Si_3N_4 by an in-situ direct nitridation process [41]. The nanocomposite was found to have a higher electrical conductivity because of the formation of a continuous network of TiN. Zhang *et. al.* modulated the intensity and the position of optical absorption bands by means of assembling the porous $A1_20_3$ host with nano-Cr_20_3 particles and heating in H_2 [42].

2.7 Synthesis of nanomaterials

The synthesis of NsM materials is usually done following two approaches

1. Bottom-up approach
2. Top-down approach

Bottom-up approach consists of chemical synthesis, chemical vapor deposition, thermal spray technique, inert gas condensation, rapid solidification and electrodeposition. Bottom up synthesis approach use the phenomenon of assembly of atoms or particles Top-down approach consists of processes like mechanical alloying/milling, wear, devitrification and spark erosion.

Chemical reactions for material synthesis can be carried out in the solid, liquid or gaseous state [43]. Use of wet chemical synthesis processes result in fast diffusion of matter in the liquid phase which is several times faster than solid phase, thus leading to synthesis of nanostructured materials at low temperatures. Vapor condensation or evaporation processes consist of heating a metal or chemical to high temperatures under high vacuum conditions. The vaporized atoms collide with each other in the high vacuum chamber and lose the kinetic energy and condense in the form of powder. The powder size and morphology depends on process variables like substrate temperature and vacuum conditions. Fine powders produced can be allowed to react with gases to form oxides, nitrides, carbides, sulphides etc.

2.7.1 Sol gel process

Sol gel process uses precursors or starting compounds for preparation of a colloid consisting of a metal or a metalloid element surrounded by various ligands. It involves hydrolysis and condensation of precursors traditionally metal alkoxides. The condensation reaction leads to the formation of gel. Sol gel processes can be used to prepare a variety of material like powders, films, fibers, glass and monoliths. Processing variables that need to

controlled in a sol gel process which can effect the kinetics, growth and condensation reactions are:

a) solvent

b) temperature

c) precursors

d) pH

e) additives and

f) mechanical agitation

2.8 Sintering of nanopowder

Synthesis, characterization and processing of nanocrystalline materials are part of a rapidly emerging and fast growing field of nanoscience and nanotechnology. Nanocrystalline materials show several interesting properties due to one or several of the following reasons [36]. Ceramic nanostructures has changed the approach to materials design in many applications by seeking structural control at atomic level and tailoring of the engineering properties[44]. As the particle size decreases a higher proportion of atoms reside at the interfaces i.e. either the free interfaces (surface) or the internal interfaces (grain boundaries) (Figure 8 a, b). The boundaries can be considered as defects where a misfit between adjacent crystallites changes the atomic structure (the average atomic density, coordination number etc) relative to a perfect crystal. Hence, more atoms have coordination number different from atoms at the grain interiors. Since bonding and interaction among the constituent atoms play a significant role in deciding the properties of a material a lower coordination number for a increased number of atoms results in material properties for nanomaterials different from their bulk counterparts.

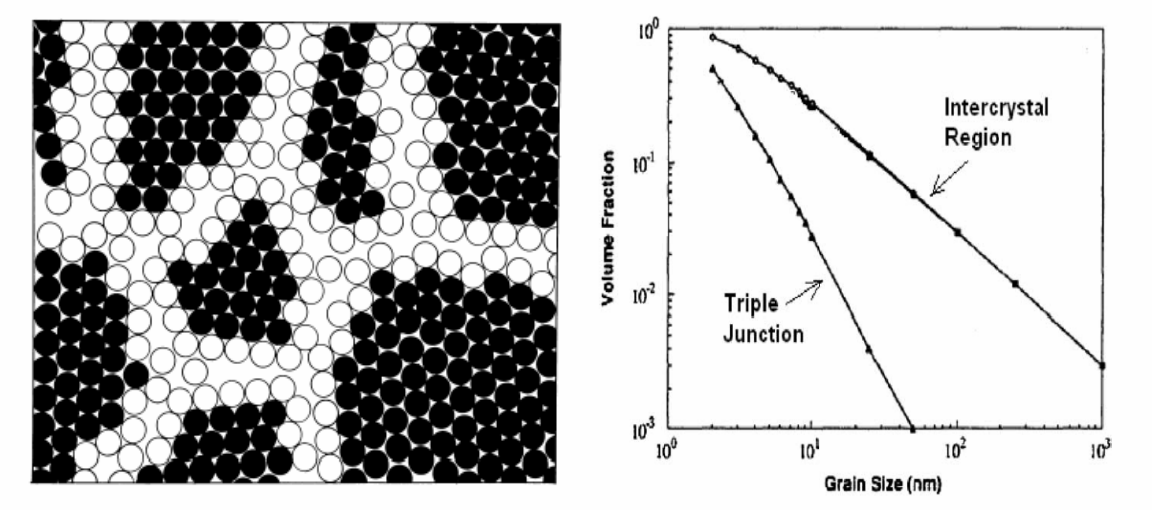

(a) **(b)**

Figure 8. (a) Atomic structure of a nanostructured material developed by computational modeling. The black atoms are atoms the sites of which deviate by more than 10 % from the corresponding lattice sit. (b) Effect of grain size on calculated volume fractions of intercrystal regions and triple junctions, assuming grain boundary width of 1 nm. Adapted from Gleiter.

The main goal during sintering of nanomaterials is to retain their nanosized (< 100 nm) and their unique features that nanoscience offers. Nanosintering presents challenges due to following reasons [45]:

1. Particle agglomeration,
2. High reactivity and inherent contamination,
3. Grain coarsening and
4. Ultimate loss of the nanofeatures.

Decrease in particle size results in an increase in the surface area and consequently an increase in the surface free energy. The large surface area renders the nanoparticles unstable.

This leads to nanoparticles adopting different surface energies than regular ones, for instance, by a different local atomic arrangement at the surface. TEM studies showed that nanoparticles have a faceted appearance with anisotropic surface energies. Kinetically, sintering of nanopowders is significantly enhanced because of the higher surface energies. Therefore, sintering of a number of nanoparticles indicated depressed sintering onset temperatures (0.2-0.3 T_m) as compared to conventional powders (0.5- 0.8 T_m) [46]. Molecular dynamics (MD) simulations indicated extremely fast sintering of nanoparticles.

Nanomaterials tend to agglomerate to reduce the surface energy. Major challenges in processing of nanopowder includes producing bulk quantity of nanopowder with minimal or no agglomeration [47]. Problems arise during powder compaction due to presence of hard agglomerated particles, high plastic yield, resistance to motion under pressure and contamination of particle surfaces. Compaction by conventional processes involves certain amount of sliding and rearrangement, both of which become increasingly difficult as particle size decreases. On the nanoscale, the frictional forces between particles become a very significant obstacle to their relative motion and rearrangement.

CHAPTER THREE:

METHODOLOGY

3.1 Raw materials used

Table 4 gives details of the purity and source of the precursors and chemicals used in this study.

Table 3. Chemical precursors used in the study.

Chemical precursors	Purity	Company/Source
Aluminum isopropoxide	reagent grade	Fisher Scientific, USA
Titanium (IV) isopropoxide	98+%	Fisher Scientific, USA
Propanol	1 N	Alfa Aesar
Hydrochloric acid	1 N	Alfa Aesar

3.2 Synthesis of powder nanocomposite

Al_2O_3- Al_2TiO_5-TiO_2 nanocomposite powder was synthesized using aluminum isopropoxide, and titanium (IV) isopropoxide as precursors for aluminum and titanium respectively. Propanol was used as solvent and hydrochloric acid was used to control the pH of the solution. 20ml of propanol was heated in a beaker to 50°C. Stoichiometric amount of aluminum isopropoxide was added into hot propanol and refluxed at 120°C for 2 h. The solution was allowed to cool to room temperature in atmospheric conditions. Stoichiometric amount of titanium (IV) isopropoxide was dissolved in 5 ml propanol separately. The precursors were

added in proportions such as to allow complete formation Al_2TiO_5. The aluminum isopropoxide solution, taken in a burette, was added drop-wise in the titanium (IV) isopropoxide-propanol solution with continuous stirring. pH of the solution was continuously monitored throughout the process. Hydrochloric acid was added to maintain the pH of the solution at 5.5 during the process. The Al-Ti solution was refluxed at 120°C for 2 h. Refluxing was done to allow for heating the specimen and complete mixing of the precursors without letting the solvent to evaporate. The resulting solution was filtered and heated to 200°C in furnace atmosphere for 2 h to obtain fine dry powder. The as- formed amorphous powder was heated to 400°C for 2 h and then calcined at 700°C and 900°C in furnace under atmospheric conditions, for crystallization.

3.2.1 Effect of pH on synthesis of powder

In order to study the effect of pH on the synthesis and phase evolution of the composite powder, three different pH solutions at 3.5, 5.5 and 7 were used during synthesis. After analyzing the XRD results it was decided to work with the nanocomposite powder synthesized with solution pH of 5.5.

3.3 Gel Characterization

3.3.1 Differential Scanning Calorimetry / Thermal Gravimetric analysis

The as-formed gel was characterized using DSC and TGA to study the thermal properties and decomposition temperatures of various species at different temperatures. The gel specimen was placed in the specimen holder of the DSC / TGA analyzer (Model SDT Q600 from TA Instruments, Inc.) and heated from ambient temperature to 1500°C at a heating rate of 6°C/min.

with argon used as purging gas.

3.4 Characterization of the calcined nanopowder

Structural analysis, phase evolution, phase transformation and morphological characterization of the calcined powder was carried out using X-Ray Diffraction and Transmission Electron Microscopy (TEM).

3.4.1 X-Ray Diffraction

XRD analysis was performed to study the phase evolution, crystal structure(s) and crystallite size(s) of the phase(s). XRD images of powder calcined at different temperatures were recorded using a Rigaku-DXR 3000 X-Ray diffractometer using Ni filtered CuKα radiation (λ =0.1542 nm) at 40 kV and 40 mA settings.

Phase evolution and grain sizes of the specimens were investigated. To qualitatively analyze the percentage of AT present in the heat treated powder, we compared their 100% peak intensity calculated using XRD data using the equation:

% phase I = 100 X [(maximum peak height of phase I) / (∑ maximum peak heights of various phases present)] **(**Equation 1)

Full width at half maximum (FWHM) as determined by X Ray diffraction was used to calculate and compare the grain size of powder specimens heat treated at 1200°C, 1300°C and 1400°C for 2 h and 6 h respectively (Table 1). To accurately calculate the sizes of small grains it is necessary to first subtract the peak broadening due to lattice strain and the instrument [[48]]. An

accurate estimate of the peak broadening due to grain size alone is given by:

$$\mathbf{B_r^2 = B_o^2 - B_i^2} \qquad \textbf{(}\text{Equation 2)}$$

Where $\mathbf{B_r}$ is the width due to combined effects of crystallite size and lattice strain, $\mathbf{B_o}$ is the observed peak width and $\mathbf{B_i}$ is the width due to instrumental effects. All the peak widths were measured in radians at an intensity called half the maximum value called full width at half maximum (FWHM). The value of $\mathbf{B_r}$ as calculated was then used in the Scherrers equation given by:

$$\mathbf{B_{crys} = (k\,\lambda) / (L\cos\theta)} \qquad \textbf{(}\text{Equation 3)}$$

Where λ is the wavelength of the X-Ray used (1.5406 A^o), θ is the Bragg angle, k is a constant and L is the average crystallite size measured in a direction perpendicular to the specimen. In order to find B_i we conducted the XRD of a pure AT powder specimen annealed at 700°C for 45 min after heat treatment at 1500°C for 6 h. The obtained powder was coarse grained with minimum strain and hence the peak width of the XRD plots can be considered to be due to the instrument effect (B_i) alone. The calculated B_i and as-obtained B_o were used to calculate B_r and finally the grain size.

3.4.2 Transmission Electron Microscopy

High resolution transmission electron microscopy was conducted to analyze the grain size and particle morphology using a FEI Tecnai F30 TEM. It has a resolution of 0.20 nm point to point and can capture images with a maximum magnification of 10,000,000X. It operates with a field emission gun and can operate at a maximum voltage of 300 KV.

The purpose of using TEM was to confirm the presence of crystalline phase and to

analyze the microstructural details of the particles. The presence of crystalline planes was confirmed by the presence of well defined dots and ring patterns whereas amorphous phase result in halo or diffuse rings in a selective area diffraction pattern (SAED).

3.5 Powder compaction

Powder heat-treated at 400°C for 2 h were used as starting material for compaction and sintering studies. Cold compaction was used to press the powder into disc shaped pellets.

3.5.1 Cold uniaxial compaction

Ceramic powders were compacted by traditional cold die compaction method and then sintered at various temperatures. During cold die compaction the powder is densified by rearrangement including sliding and rolling of powders. Since nanoceramic powders have a tendency to form agglomerates it is sometimes necessary to grind the powder to break the agglomeration.

The specimens were compacted in a uniaxial single action manual hydraulic press (Carvar Press Inc, USA) using stainless steel die with internal die diameter of 12.5 mm. A dry P.T.F.E film (made with Dupont Krytox) was sprayed on the inside surface of the steel mold and punch to reduce the friction between the fine powder and metal surfaces. Uniaxially compacted green pellets, with average dimensions of 12.5 mm in diameter and 3.0 mm in thickness, were then used for sintering.

3.5.2 Sintering of compacted structures

The pressed disc shaped pellet structures were sintered in a high temperature programmable muffle furnace in ambient atmosphere and at different temperatures - 1000°C, 1100°C, 1200°C, 1300°C, and 1400°C for 2 h and at 1200°C, 1300°C, 1400°C and 1500°C for 6 h. A heat treatment cycle was developed based on DSC / TGA analysis to allow better densification. As-prepared gel was dried at 200°C for 2 h and then heat-treated at 400°C for 2 h. The agglomerated heat-treated powder was ground in a mortar and pestle and pressed into disc shaped pellet structures. The compacted pellets were used in muffle furnace for densification studies. Pellet structures were heated to 400ºC at a heating rate of 8ºC/min and homogenized at this temperature for 30min. In the second step, temperature was increased to the desired final temperature at a slower heating rate of 4ºC/min. Pellets were cooled to room temperature at 10°C/min. Three AT specimens were heat-treated at each sintering temperature and the values reported are average of the three samples. Geometric bulk density (ρ_g) of each pellet was evaluated from the measurements of the mass of specimen and its volume (determined by dimensional measurements) using the following equation.

Bulk Density = Mass / Volume (Equation 4)

3.6 Characterization of sintered pellet structures

3.6.1 Phase analysis

The pellet structures sintered at 1000ºC-1500ºC were ground in a mortar and pestle and used for XRD analysis to study the phase composition, phase purity and grain size of the nanocomposites as described in section 3.4.1.

3.6.2 Scanning Electron Microscopy

SEM provides high magnification images of solid materials with a high depth of field. SEM images of the pellet structures sintered at various temperatures were recorded using a Hitachi S800 SEM. The equipment uses a cold emission electrode source, is an ultra high-resolution scope and has resolution of 2 nm and a maximum magnification of 300000X. It can accommodate specimens up to 25 mm in diameter and 20 mm in height. All the images were captured in the secondary electron mode and Genesis software was used to capture images. The SEM images were captured to investigate the microstructure and grain size.

3.6.3 Mechanical Characterization

Mechanical properties of sintered pellet structures were evaluated by measuring their Vicker's hardness number and biaxial flexural strength. Hardness of the sintered specimens was characterized using a Vicker's hardness tester (Model LV-700, Leco Corporation, St. Joseph, MI). Average dimensions of the specimens used for hardness measurements were 9 mm in diameter and 1.8 mm in thickness. Two samples, compacted at 162 MPa, sintered each at 1300°C, 1400°C and 1500°C temperatures were used for the study. 3 indentations on each specimen were measured to calculate the hardness values.

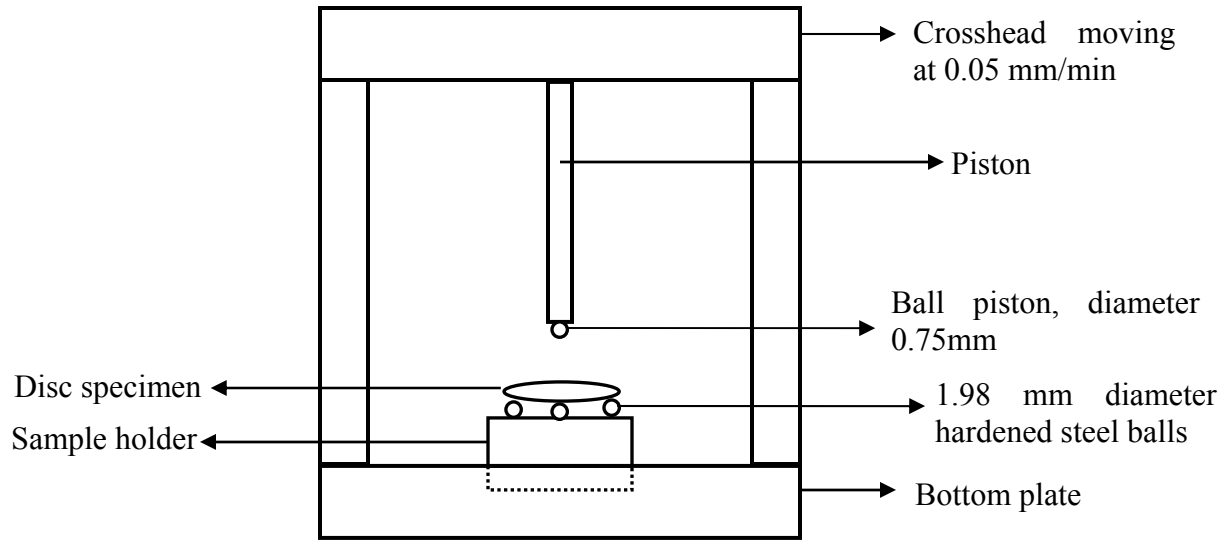

Figure 9. Schematic of the biaxial flexure test fixture used in the study.

A flat ended ball piston (0.75 mm in diameter), pressing against a three ball (1.98 mm in diameter) test jig was used for the biaxial flexural test of circular disc shaped sintered specimens. To closely mimic the ASTM F 394-78 standard the 3 ball test jig was fabricated using hardened steel balls but the dimensions of the ball and test specimens were smaller than that specified in ASTM standard.

Sintered disc specimens were centered and supported on three hardened steel balls positioned 120° apart on a circle, 7.5 mm in diameter. A thin plastic coated thick paper sheet was placed between the specimen and flattened ball piston to distribute the load evenly. The specimens were tested on an Instron Testing Machine with a crosshead speed of 0.05 mm/min. The recorded fracture load was used to calculate the biaxial fracture strength using the following equations:

$$S = -0.2387\ P\ (X-Y)/d^2 \qquad \text{(Equation 5)}$$

where S is maximum center tensile stress in MPa.

P is the total load causing fracture in N.

$X = (1+\nu)\ \ln (B/C)^2 + [(1-\nu)/2](B/C)^2$

$Y = (1+\nu)\ [1+ \ln (A/C)^2\ ]+ [(1-\nu)](A/C)^2$

μ is poisons ratio (taken as 0.27)

A is radius of support circle in mm.

B is the radius of loaded area or ram tip in mm.

C is the radius of specimen in mm.

d is specimen thickness at fracture origin in mm.

3.7 Assessment of bioactivity

The bioactivity of sintered Al_2O_3-TiO_2-Al_2TiO_5 structures was investigated by monitoring their weight loss and change in pH as a function of time in a protein-free dynamic simulated body fluid (SBF). SBF has been used widely by researchers to test bioactivity of materials, by examining the formation of an apatite layer on the surface of testing materials. The *in vivo* formation of an apatite layer on the surface of a bone-grafting material can be reproduced in acellular SBF which is prepared to have an ion concentration nearly equal to that of human blood plasma. It should be also noted here that SBF is a solution highly supersaturated with respect to apatite. It is not easy to prepare clear SBF with no precipitation. In this work we have used SBF prepared according to the detailed recipe reported by Kokubo ***et. al*** [49].

3.7.1 Preparation of simulated body fluid

The following chemicals were used to prepare the SBF. The fluid was prepared in a plastic container and deionized water was used for preparation.

1. sodium chloride (NaCl)
2. sodium hydrogen carbonate ($NaHCO_3$)
3. potassium chloride (KCl)
4. di-potassium hydrogen phosphate trihydrate ($K_2HPO_4.3H_2O$)
5. magnesium chloride hexahydrate ($MgCl_2.6H_2O$)
6. calcium chloride ($CaCl_2$)
7. sodium sulphate (Na_2SO_4)
8. tris-hydroxymethyl aminomethane
9. 1 N hydrochloric acid
10. pH standard solution (pH 4 and 7).

The ion concentrations of SBF are shown in table 5. 500 ml of SBF was prepared in a clean, scratch free plastic container. The entire process was carried out in a temperature of 34°C-38°C under continuous stirring. The reagents were dissolved in sequence from serial number 1 to 8 as mentioned above. Precaution was taken to add a reagent only when the preceding reagents had dissolved completely. The last two reagents were dissolved in order to maintain the Ph throughout the process.

Specimens sintered at 1400°C, 6 h were used for the SBF study. 9 specimens were used in total for studying the weight loss, Ph and biaxial flexural strength. 3 specimens were used for tests every week. Specimens taken out after first and second week were used for SEM, EDX and

XRD investigation to confirm the formation of apatite.

3.8 Measurements of dielectric properties

Dielectric properties were measured on pellets sintered at temperatures in the range of 1000°C to 1400°C. Silver paste (electrode) was applied on both sides of the sintered pellets and the structure was dried at 400°C for 30 min. These structures were used to measure the capacitance and dissipation factor at 1 MHz using Agilent 8284A precision LCR meter and 16451 B dielectric test fixtures. The capacitance (C) of the pellet structures was then used to calculate the dielectric constant using the equation:

$$C = A\varepsilon_o / d \qquad \text{(Equation 6)}$$

Where A is the area of the pellet, d is the thickness of the pellet and ε_o is the dielectric constant of vacuum. The sintered pellets (without silver paste) were grinded and used for XRD analysis.

3.9 Rietveld refinement of X-Ray Diffraction data

The diffraction data of nanocomposite powder sintered at 1400°C for 6 h was qualitatively analyzed using Rietveld refinement technique to investigate the phase purity of the powder, crystal structure and lattice parameter(s) of the phase(s) present. Rietveld analysis was carried out using General Structural Analysis System (GSAS) which is a set of programs for the processing and analysis of powder diffraction and single crystal data both by x rays and neutron diffraction. Structural data used during the refinement was based on the details provided by Lekanova *et al.*[50] The refinement was obtained by varying the scale factor, lattice parameters (a, b and c), grain size and background coefficients.

Table 4. Nominal ion concentration of SBF in comparison to human blood plasma.

Ion	**Ion concentrations (mM)**	
	Blood Plasma	**SBF**
Na^+	142	142
K^+	5.0	5.0
Mg^{2+}	1.5	1.5
Ca^{2+}	2.5	2.5
Cl^-	103	147.8
HCO_3^-	4.2	4.2
HPO_4^{2-}	1.0	1.0
SO_4^{2-}	0.5	0.5
Ph	7.4	7.4

CHAPTER FOUR:

RESULTS

4.1 Effect of pH on crystallization of the powder.

The powder synthesized at three different pH values of 3.5, 5.5 and 7.0 were analyzed using XRD (Figure 10). No distinct peaks are observed in the XRD pattern of powder synthesized employing pH of 3.5 and calcined at 700ºC for 2 h.

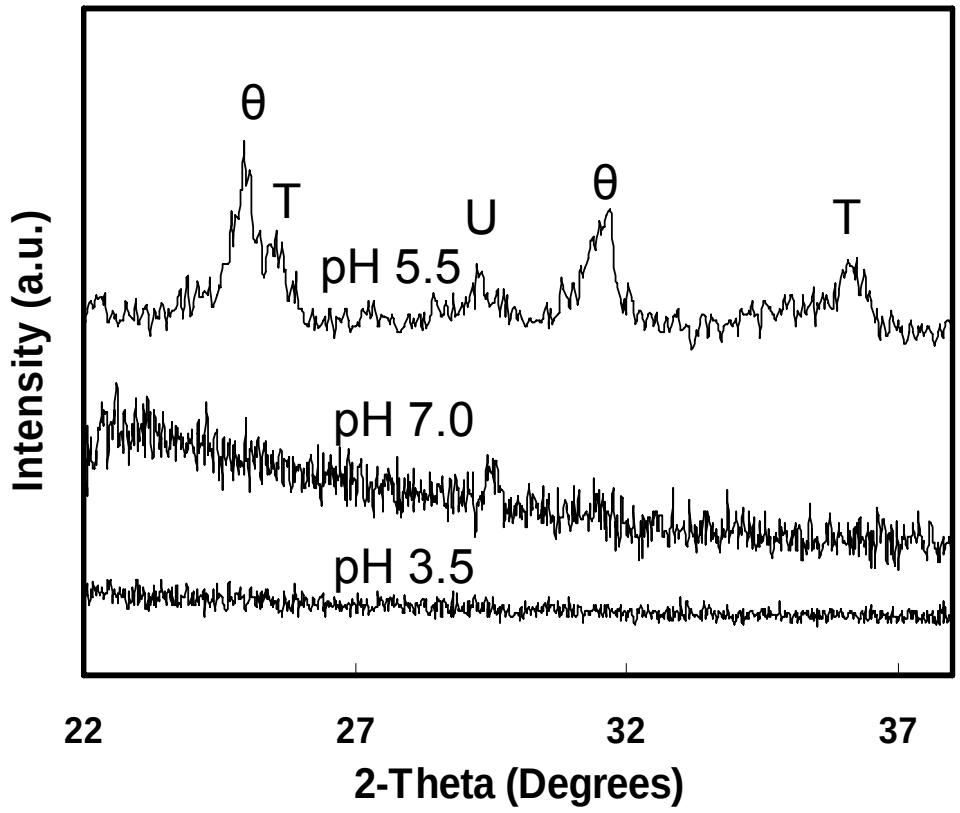

Figure 10. XRD plot of powder calcined at 700°C for 2 h synthesized in solutions at various pH. The phase present are θ-Al_2O_3 and anatase TiO_2 and an unknown phase denoted by 1, 2 and U respectively.

XRD pattern of powder synthesized with pH 7.0 shows low intensity broad peaks. XRD plot of powder synthesized with pH of 5.5 shows broad peaks of θ-Al_2O_3 and anatase TiO_2. The powders synthesized at ph 5.5 were crystalline and of very fine size. Phase analysis of the plot showed the presence of anatase TiO_2 [PDF# 00-021-1272], θ-Al_2O_3 (monoclinic crystal structure) and an unknown peak at 2θ = 29.3º. Based on the results of XRD, AT powder synthesized with pH of the solution maintained at 5.5 were used for further study.

4.2 Gel characterization

4.2.1 Differential Scanning Calorimetry & Thermo gravimetric Analysis

Figure 11 is the DSC / TGA plot of the as-synthesized gel heated from room temperature to 1500ºC. The DSC plot shows an endothermic peak at 105ºC which is followed by a broad exothermic peak in the range of 200ºC to 380ºC. Shallow endothermic peak / plateau are observed at around 720ºC and 900ºC. Further increase in temperature results in a broad exothermic peak stretching from 1120ºC to 1200ºC. The TGA plot shows that the as-synthesized gel undergoes a continuous weight loss starting from 50ºC to 328ºC. The weight loss up to this temperature is around 38%. At this point the slope of the TGA curve shows a major change. Though the weight loss continues till around 900ºC, the rate of weight loss is very low.

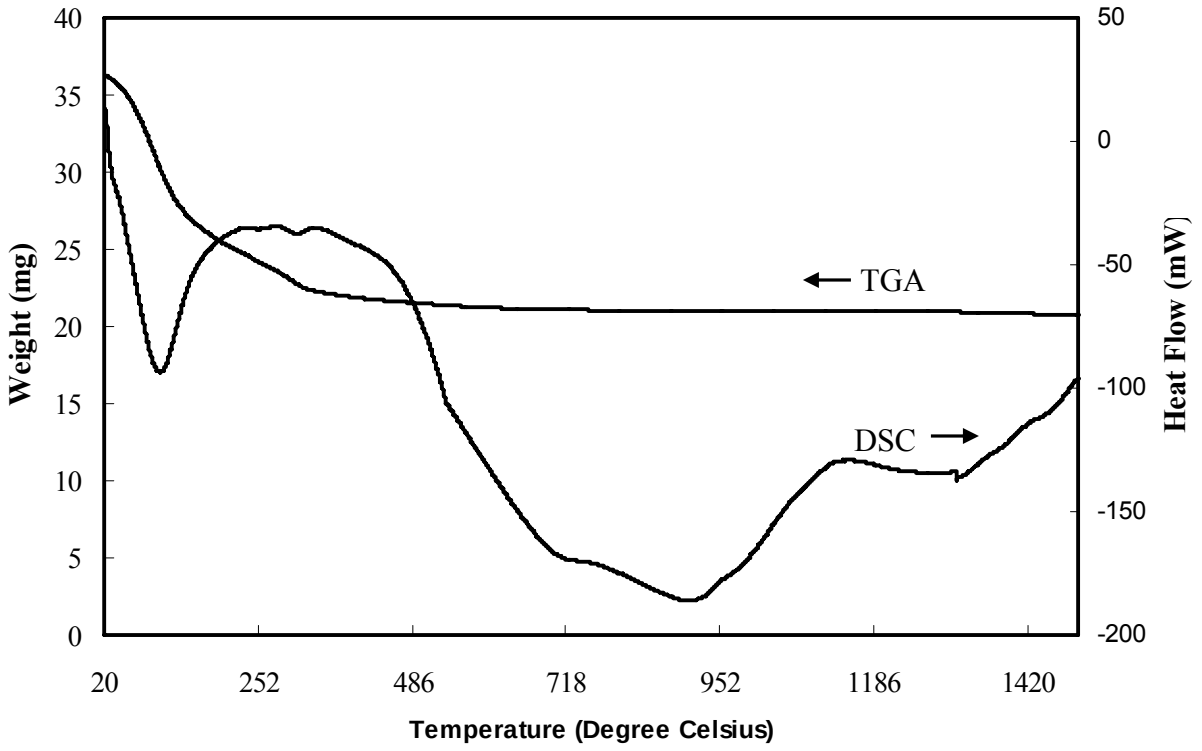

Figure 11. DSC and TGA plot of the as synthesized gel from 25ºC up to 1500ºC at 6ºC/min.

4.3 Characterization of the calcined powder

4.3.1 X-Ray Diffraction and Transmission Electron Microscopy

X-Ray powder diffraction studies were conducted on the powder specimen calcined at various temperatures to analyze the phase composition, phase purity and particle size. XRD of as synthesized powder and powder heat treated at 400°C did not show any distinct peaks indicating the amorphous nature of the powder.

Figure 12 shows the XRD plot of the powder calcined at 900°C for 2 h. Peaks observed in the plot are sharp and the phases are identified as α-alumina (α-Al_2O_3, corundum, hexagonal

crystal structure, PDF# 00-010-0173) and rutile (TiO_2, tetragonal crystal structure, PDF# 01-078-1510). The powder which had a light brown appearance after heat treatment at 400°C turned white on heating at 900°C.

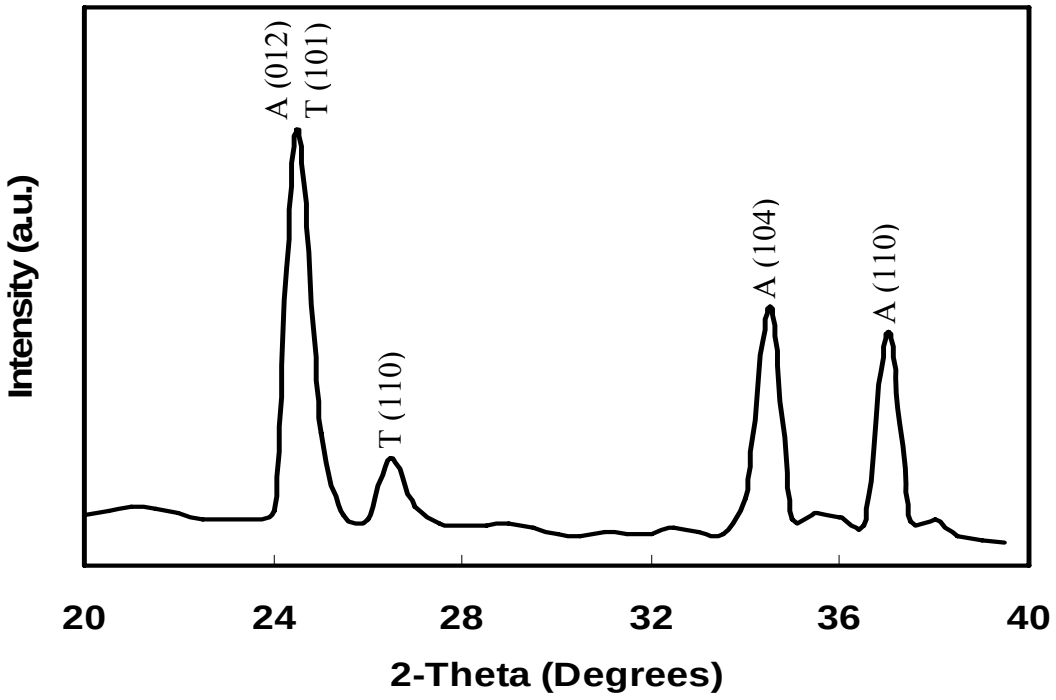

Figure 12. XRD plot of nanocomposite powder sintered at 900ºC, 2 h. The phases present are α-Al_2O_3 and anatase TiO_2 denoted as A and T respectively.

HR-TEM of the powder specimen calcined at 900°C for 2 h was conducted to analyze the grain size and morphology of calcined powder. Atomic planes and lattice fringes are visible (Figure 14) confirming the crystalline nature of the calcined powder. Grain sizes of several grains were measured and the average size was around 12 nm. Grains are mostly circular in shape.

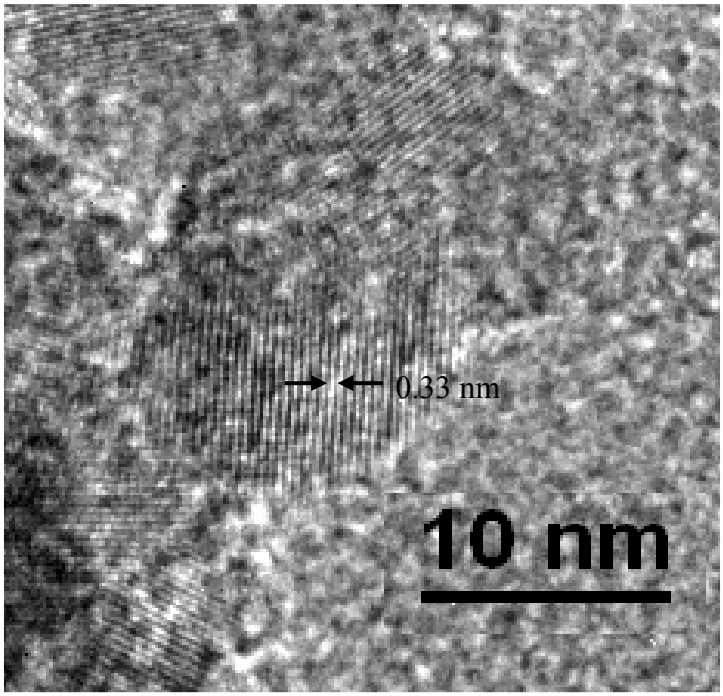

Figure 13. HR-TEM micrograph of nanocomposite powder calcined at 900^{o}C showing lattice fringes.

4.4 Sintering and densification studies

Uniaxially compacted powder pellets were sintered at temperatures 1000°C, 1200°C, 1300°C and 1400°C for 2 h and 6 h respectively. Figure 16 is the plot of variation in sintered density and volume shrinkage with increase in temperature for 2 h and 6 h respectively. Sintered density increases sharply from 1.39 g/cm^3 at 1000°C to 2.15 g/cm^3 at 1200°C. The corresponding volume shrinkage in this range almost doubles from 24% to 46% as seen in Figure 17. The sintered density is nearly constant for 1200°C and 1300°C pellets though the volume shrinkage increases from 45% to 56%. Thereafter the sintered density increases to 2.6 g/cm^3 at 1400°C and the volume shrinkage at this temperature is 62%.

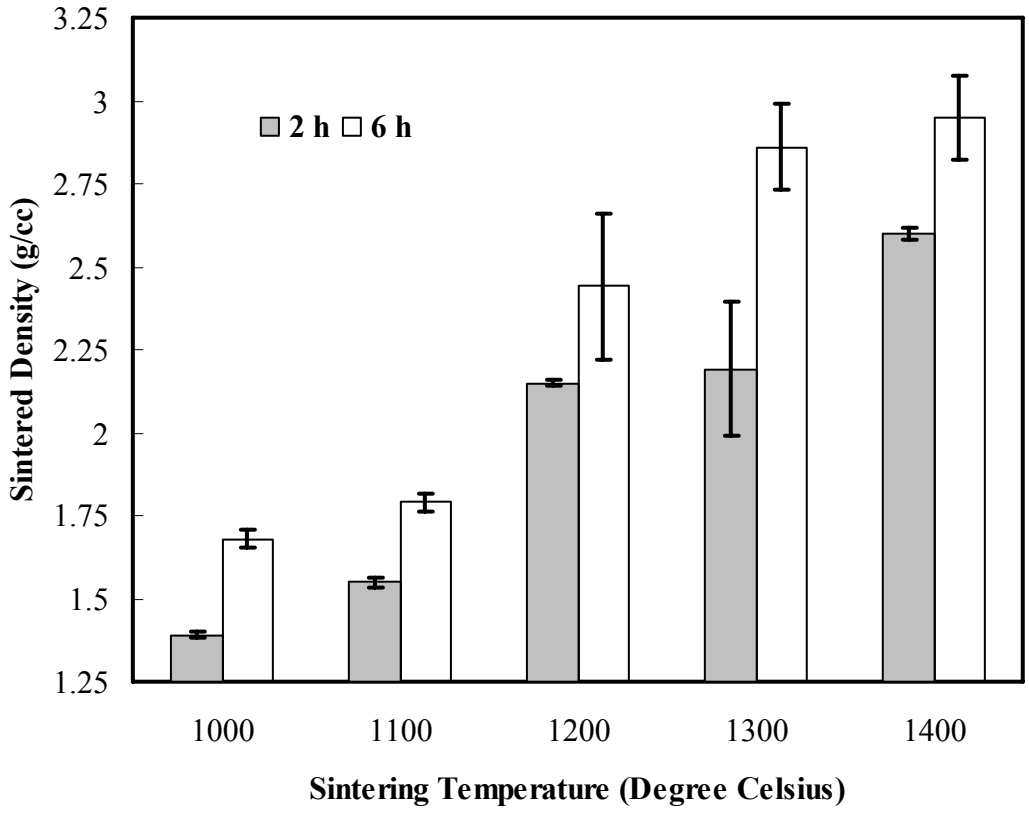

Figure 14. Density of nanocomposite pellets sintered at various temperatures for 2 h and 6 h separately. The highest density is obtained at 1400°C.

Though the density of pellets sintered for 6 h is higher than density of the pellets sintered at 2 h at all temperatures, the trend of increase in density is almost the same. The density of pellets sintered for 6 h increases from 1.68 g/cm^3 at 1000°C to 2.86 g/cm^3 at 1300°C and the highest sintered density of 2.95 g/cm^3 is obtained at 1400°C, 6 h. It is interesting to note that volume shrinkage of pellets sintered for 6 h at 1000°C (42%) is much higher than those sintered for 2 h at 1000°C (24%) but the volume shrinkage at 1400°C in both the cases is almost same.

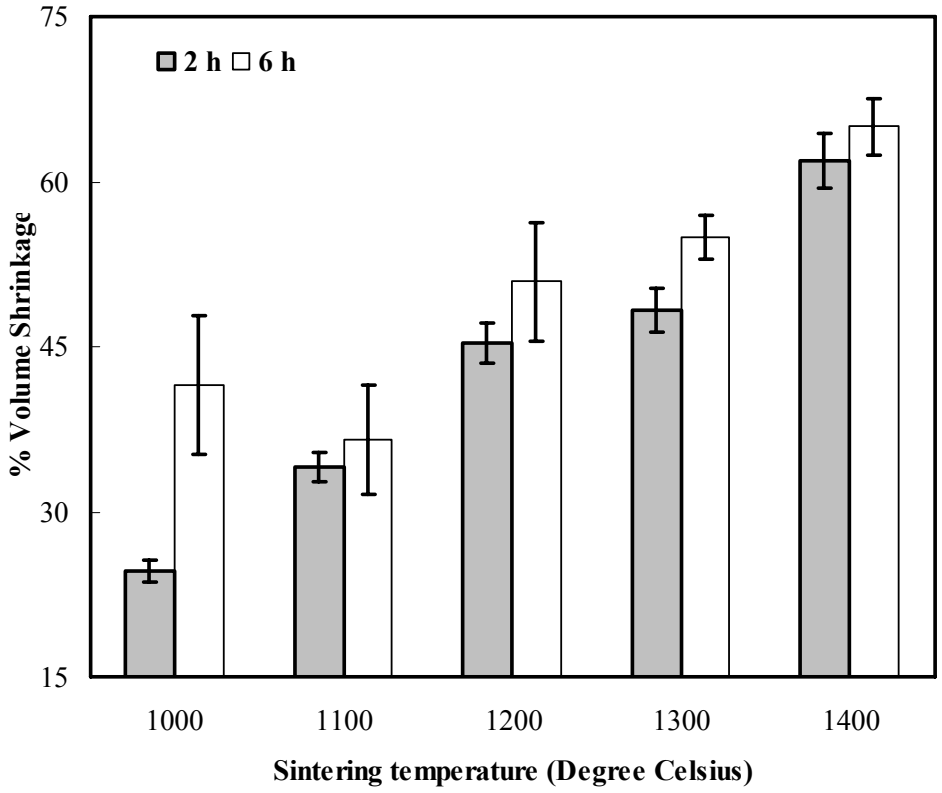

Figure 15. Percent volume shrinkage of sintered nanocomposite pellet structures for 2 h and 6 h at various temperatures.

4.4.1 Phase transformation and grain size analysis

Powder obtained by grinding pellets after sintering study at higher temperatures was used for X-Ray diffraction analysis. Phase evolution and grain sizes of the specimens were investigated. Powder heat-treated at temperatures 1000°C, 1100°C and 1200°C for 2 h is a mixture of α-Al_2O_3 and rutile TiO_2 as seen in Figure 16. Further increase in temperature resulted in formation of Al_2TiO_5 which, increased in proportion with increase in temperature. Peaks are sharp indicating that the phases have fully crystallized. No impure phase or preferential orientation is apparent.

In case of powder heat treated for 6 h at 1200°C (Figure 17), XRD analysis shows the presence of α-Al_2O_3 and rutile TiO_2 phases. Above this temperature, Al_2TiO_5 (AT) appears and the intensity of AT peaks increased on increasing the temperature from 1300°C to 1500°C. Table 5 shows the particle size of the phases present at various temperatures in pellets sintered for 2 h and 6 h.

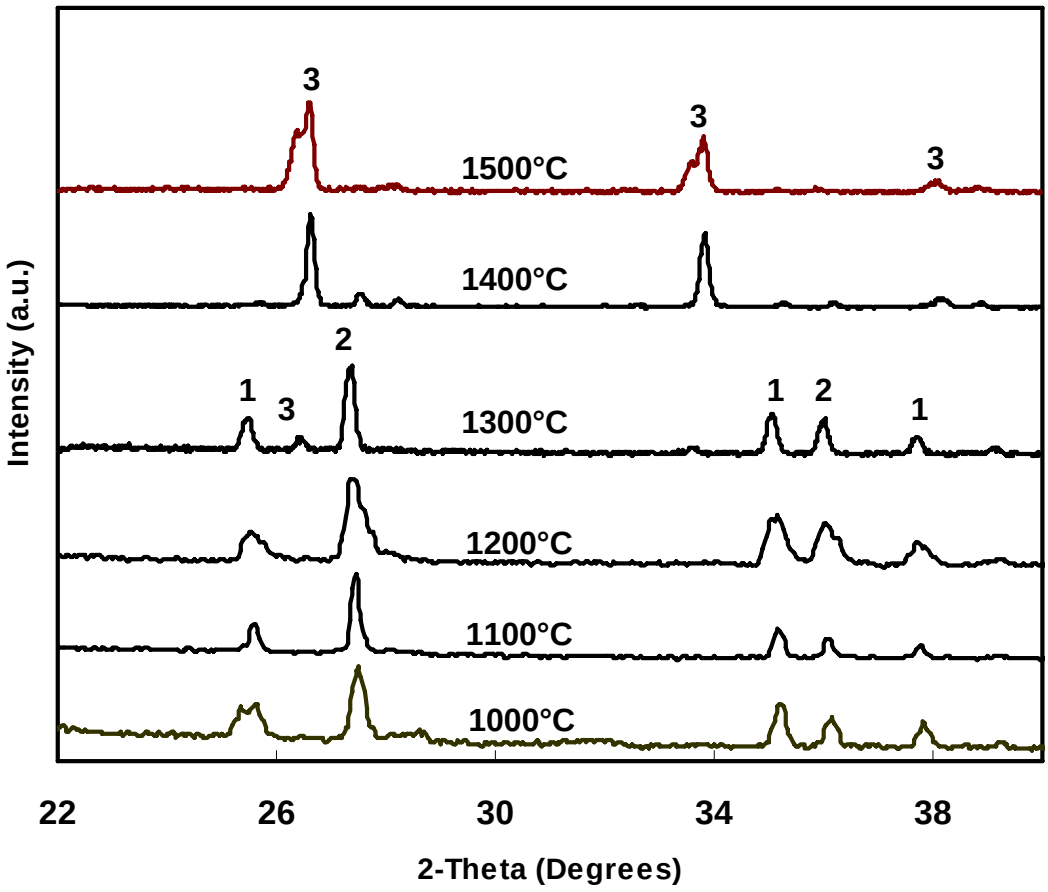

Figure 16. XRD plot of nanocomposite powder sintered at 1000ºC, 1100ºC, 1200ºC, 1300ºC, 1400ºC and 1500ºC for 2 h. Phases present are 1: α- Al_2O_3, 2: Rutile (TiO_2) 3**:** Anatase (TiO_2), 4: θ-Al_2O_3.

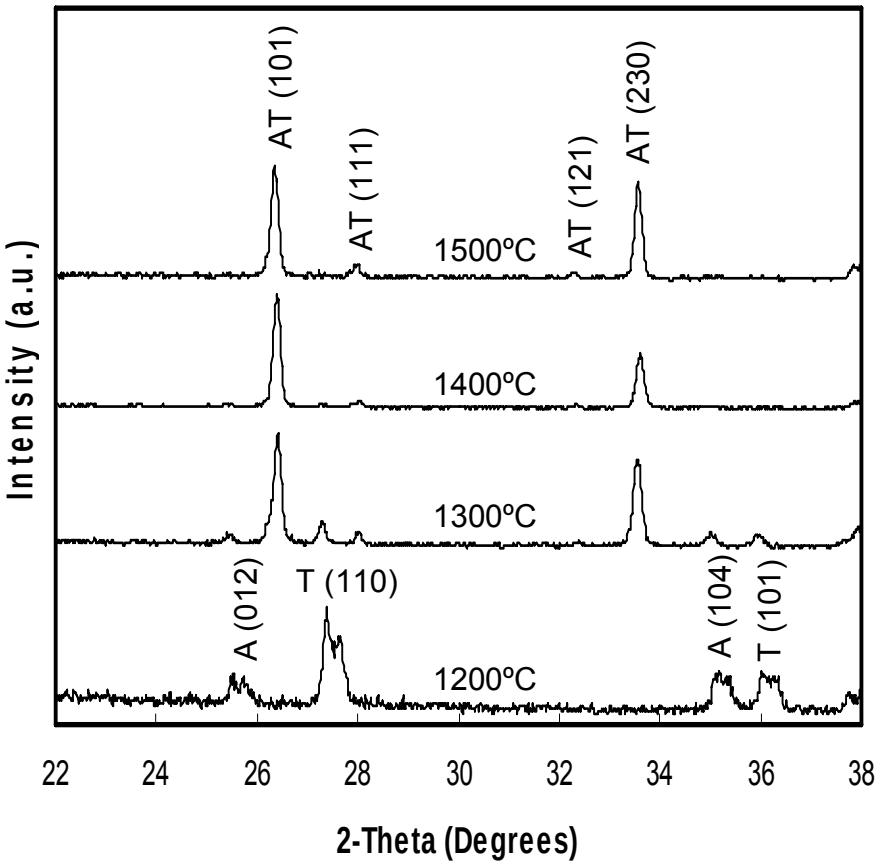

Figure 17. XRD plot of nanocomposite powder sintered at 1200ºC, 1300ºC and 1400ºC, 1600ºC for 6 h. The phases present are: Al_2O_3, (TiO_2) and Al_2TiO_5 denoted as A, T and AT respectively.

Table 5. Particle size (in nm) of various phases as a function of sintering temperature and time

	1200 ºC		1300 ºC		1400 ºC	
Time	**2 h**	**6 h**	**2 h**	**6 h**	**2 h**	**6 h**
A-Al_2O_3	24	38.6	48	100	52	-
Rutile TiO_2	24	32	45	113	55	-
Al_2TiO_5	-	-	54	66	43	92

4.4.2 Scanning Electron Microscopy

SEM images of the pellets sintered at 1300°C, 1400°C and 1500°C for 6 h are shown (Figure 18 and 19). It is obvious from the images that the particle size increases as the sintering temperature is increased. 1300°C, 6 h sintered specimens have the smallest particle size. Figure 18 shows various characteristics of sintering. The particles don't seem to have a regular morphology and irregular shaped particles can be observed.

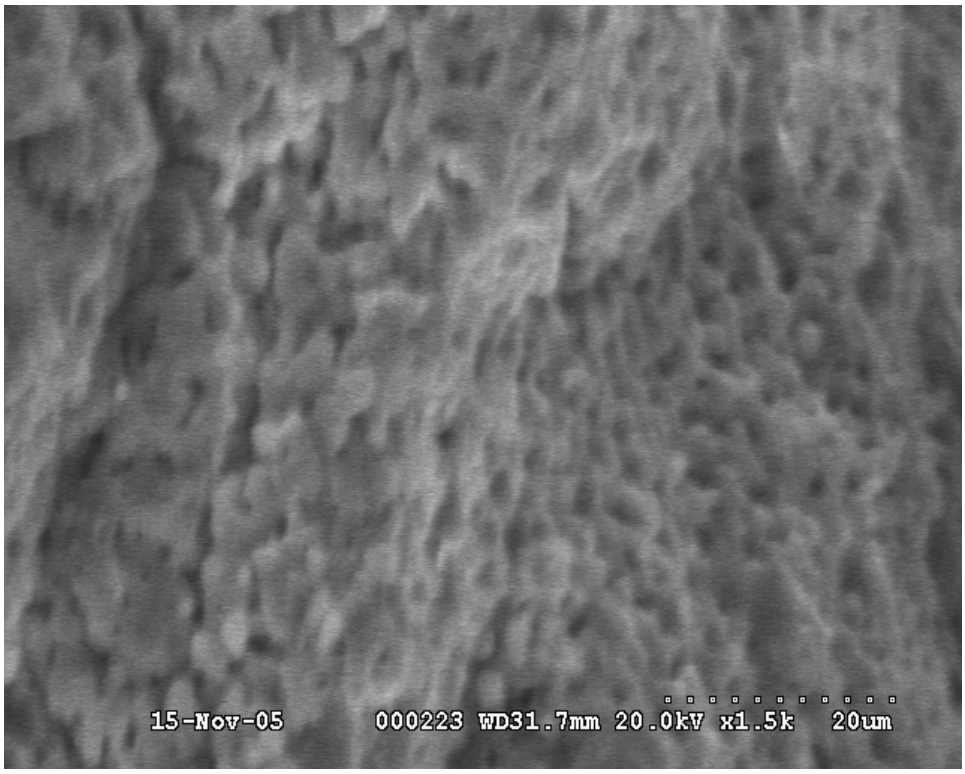

(a)

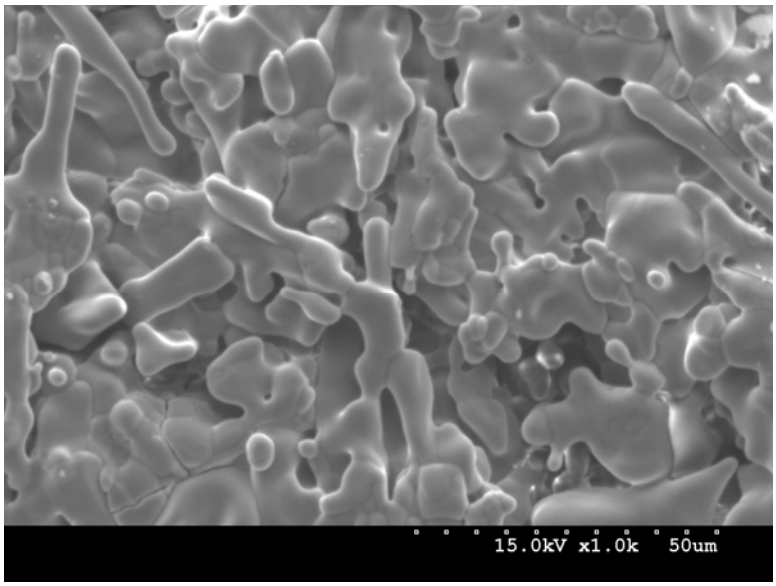

(b)

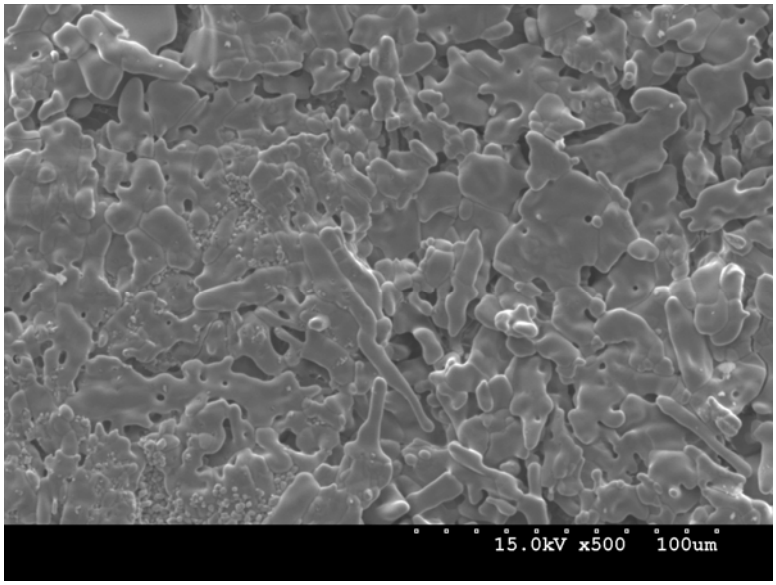

(c)

Figure 18 a, b, c. Microstructure of Al_2O_3- Al_2TiO_5-TiO_2 nanocomposite pellets sintered for 6 h at 1300°C as seen in SEM using secondary electrons.

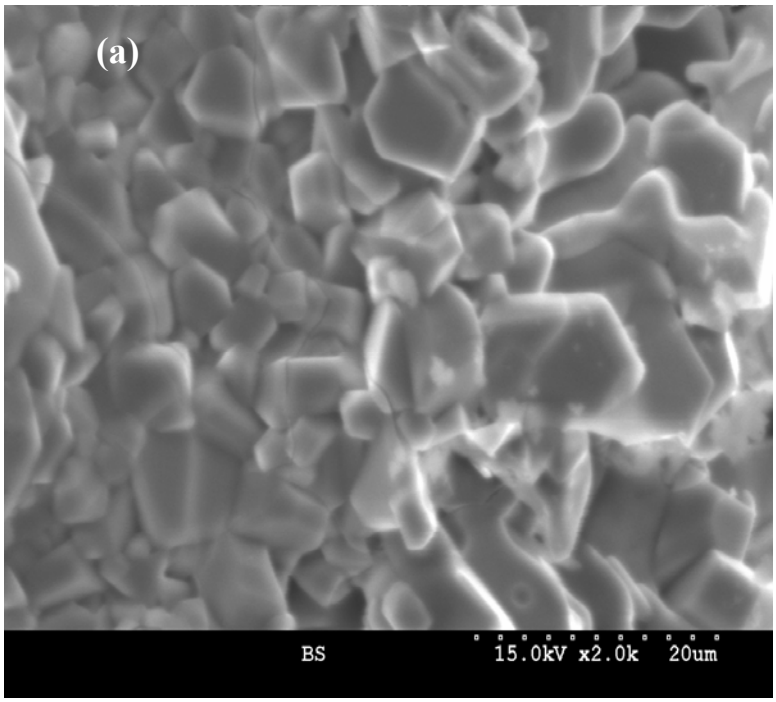

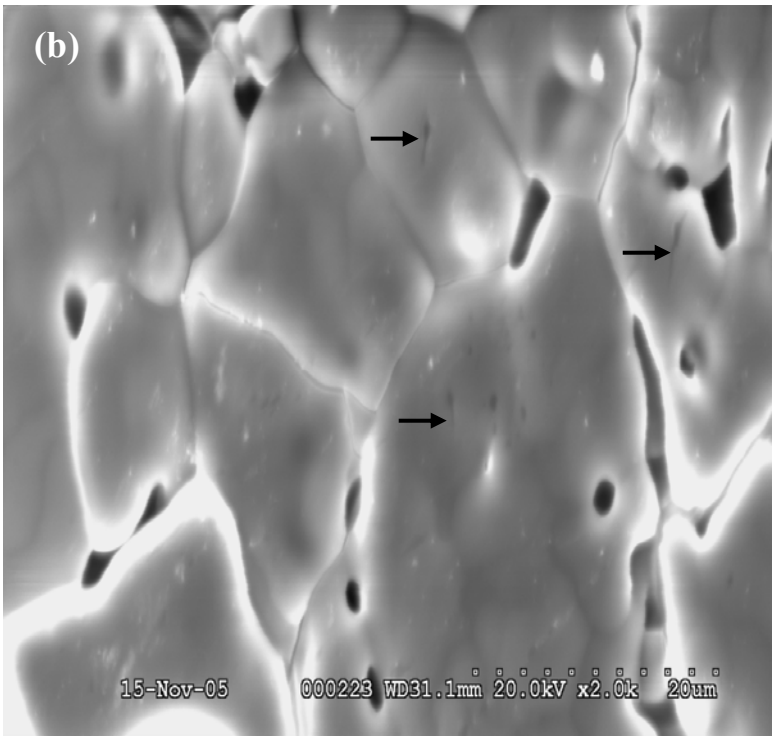

Figure 19. SEM images of Al_2O_3- Al_2TiO_5-TiO_2 nanocomposite pellets sintered for 6 h at (a) 1400°C (b) 1500°C, microcracks are shown by arrows.

4.5 Mechanical characterization

4.5.1 Vickers hardness test and Biaxial Flexure strength test

Table 7 shows the variation in Vickers hardness number and Biaxial flexure strength of specimens sintered for 6 h with increase in sintering temperature. Both Vickers hardness and Biaxial flexure strength of specimens decreased with increase in sintering temperature.

Table 6. Vickers hardness and biaxial flexure strength of disc specimens as a function of sintering temperature.

Temperature (°C)	1300°C	1400°C	1500°C
Vickers Hardness (HV)	299 (± 30.5)	234 (± 32.4)	134 (±27.02)
Biaxial Flexure Strength (MPa)	43.2 (±2.4)	15.62 (±0.8)	16.2 (±0.08)

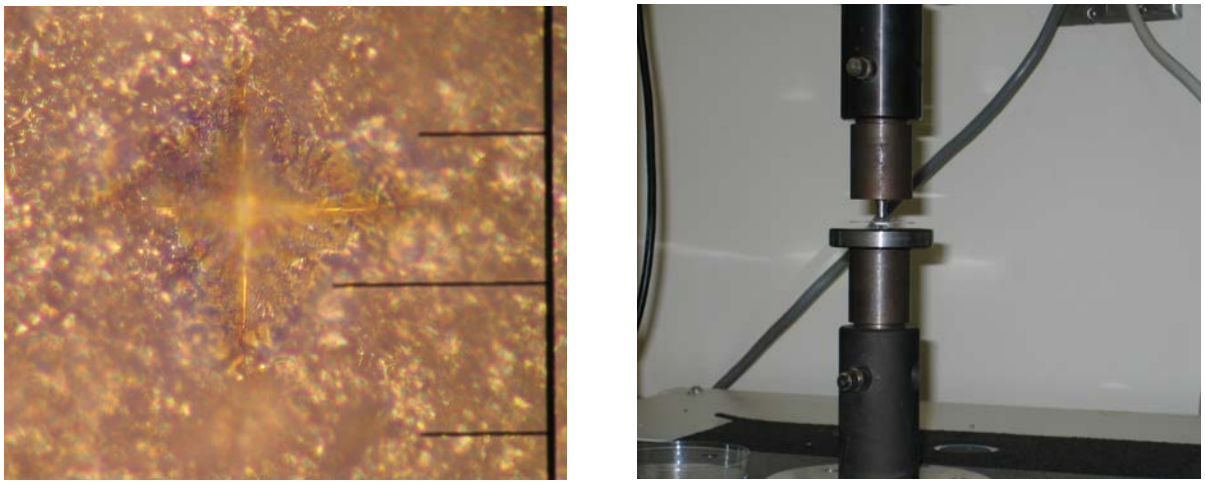

(a) **(b)**

Figure 20. (a) Vickers indentation on the pellet specimen. (b) apparatus for Biaxial flexure strength test.

4.6 Assessment of bioactivity

4.6.1 Change in pH of SBF solution and weight of pellets.

The pH of the SBF solution and the weight of sintered pellets soaked in it were monitored

after 7 and 14 days. The pH of the solution almost remained constant 7.4 to 7.53 after 7 days and to 7.55 after 14 days. There was no change in the weight of the sintered pellets.

4.6.2 SEM studies on the pellets soaked in SBF.

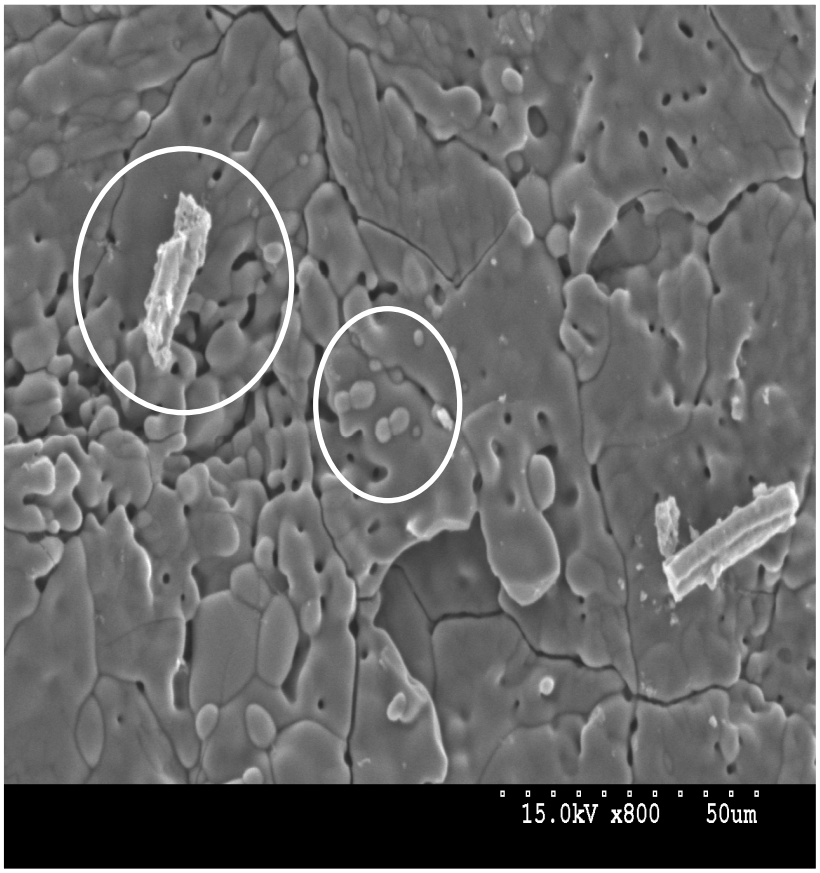

Figure 21. SEM images of sintered Al_2O_3- Al_2TiO_5-TiO_2 nanocomposite pellets soaked in SBF for 14 days shows highlighted regions with crystals of apatite in various shapes and sizes.

Figures 21, 22 and 23 show the SEM image of growing apatite crystals on the surface pellets sintered at 1400°C for 6 h and soaked in SBF for 14 days. The apatite crystals can be seen as individual particles sitting on the sintered grains of the nanocomposite (Figure 22). The sintered nanocomposite grains show characteristics like necking and larger size, associated with

a sintering process. These apatite crystals then grow in size into various shapes as shown in Figure 19. Most of the crystals have a circular shape while some of them show an elongated cylindrical structure (Figure 21).

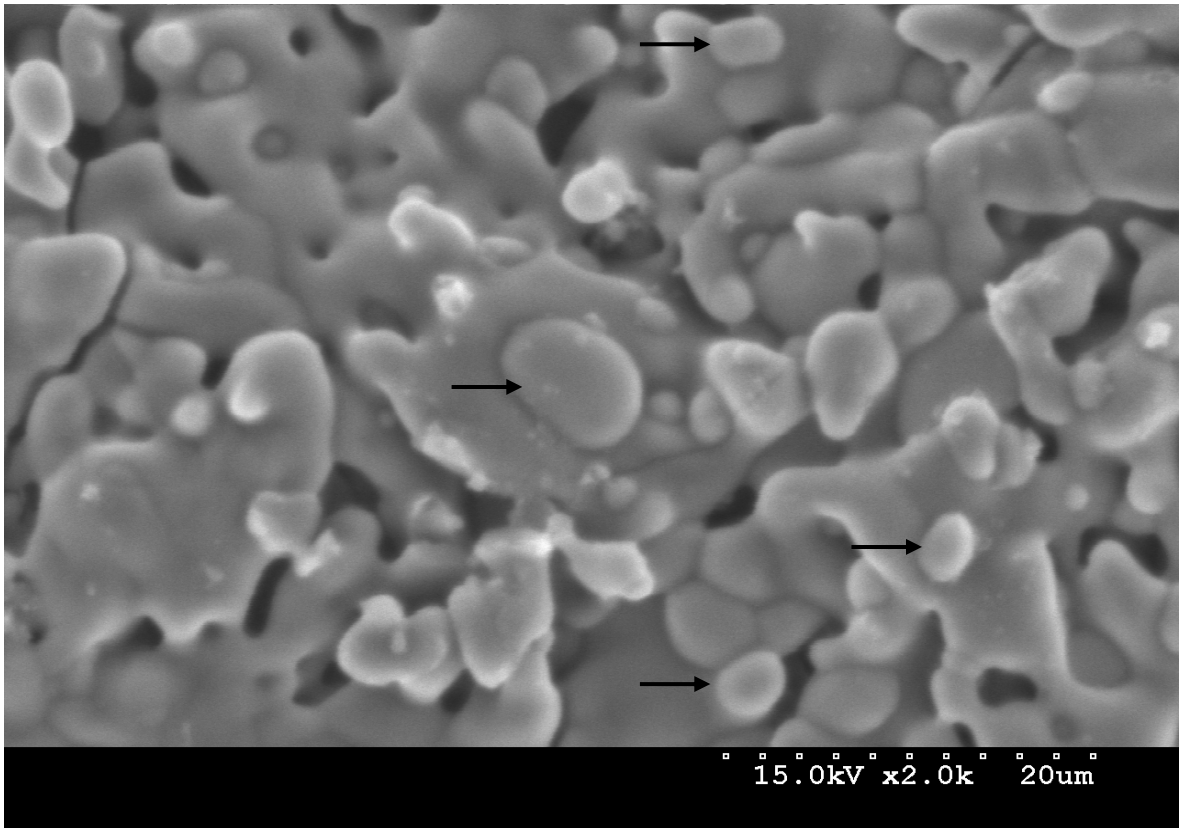

Figure 22. SEM image of Al_2O_3- Al_2TiO_5-TiO_2 nanocomposite pellet showing apatite crystal growth after soaking in SBF for 14 days. The globules are distinguishable from the nanocomposite, if one notices that the globules are sitting on the sintered grains which show necking and pores characteristic of sintering. The pellet structure was sintered at 1400ºC for 6 h.

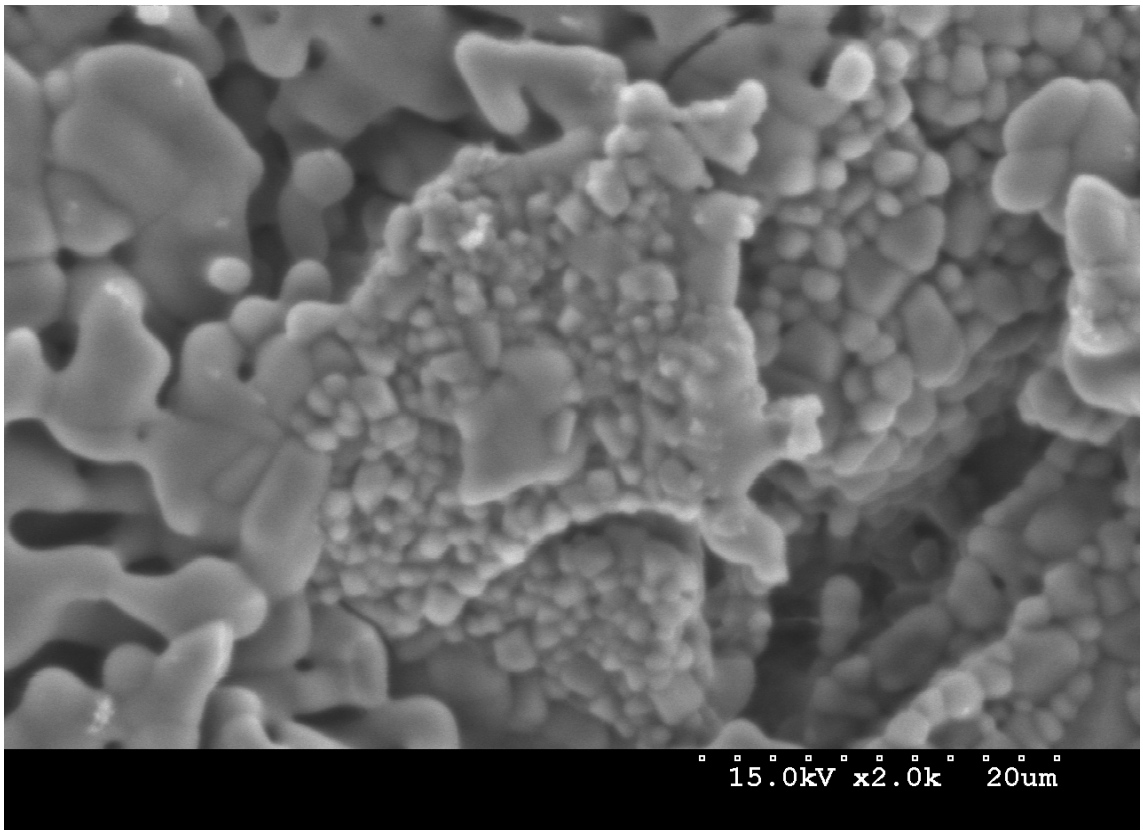

Figure 23. SEM images of Al_2O_3- Al_2TiO_5-TiO_2 nanocomposite pellet showing apatite colony formation on the surface of the nanocomposite pellet structures sintered at 1400ºC for 6 h after being soaked in SBF for 14 days. The apatite globules grow on the top sintered grains. The nanocomposite shows characteristics of sintering (necking and porosity).

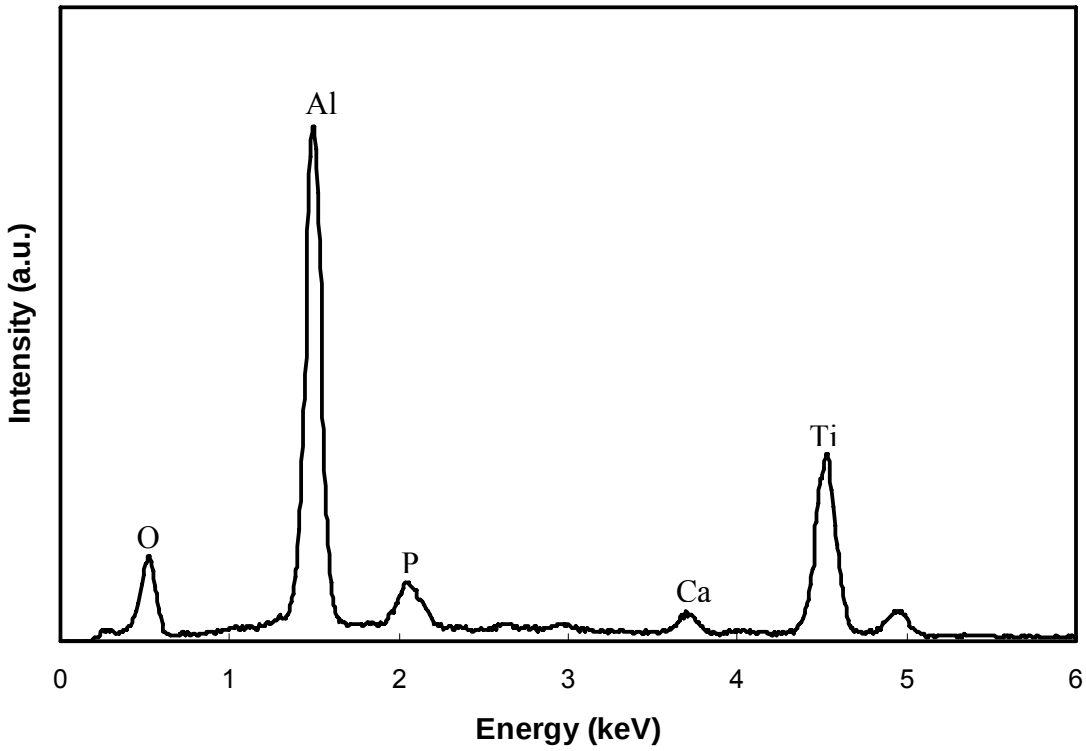

Figure 24. EDS plot of the Al_2O_3- Al_2TiO_5-TiO_2 nanocomposite pellet structure sintered at 1400ºC for 6 h after being soaked in SBF for 14 days.

Figure 24 shows the EDS plot of the pellet soaked in SBF for 14 days. Peaks of calcium and phosphorous indicate the presence apatite which is a form of calcium phosphate.

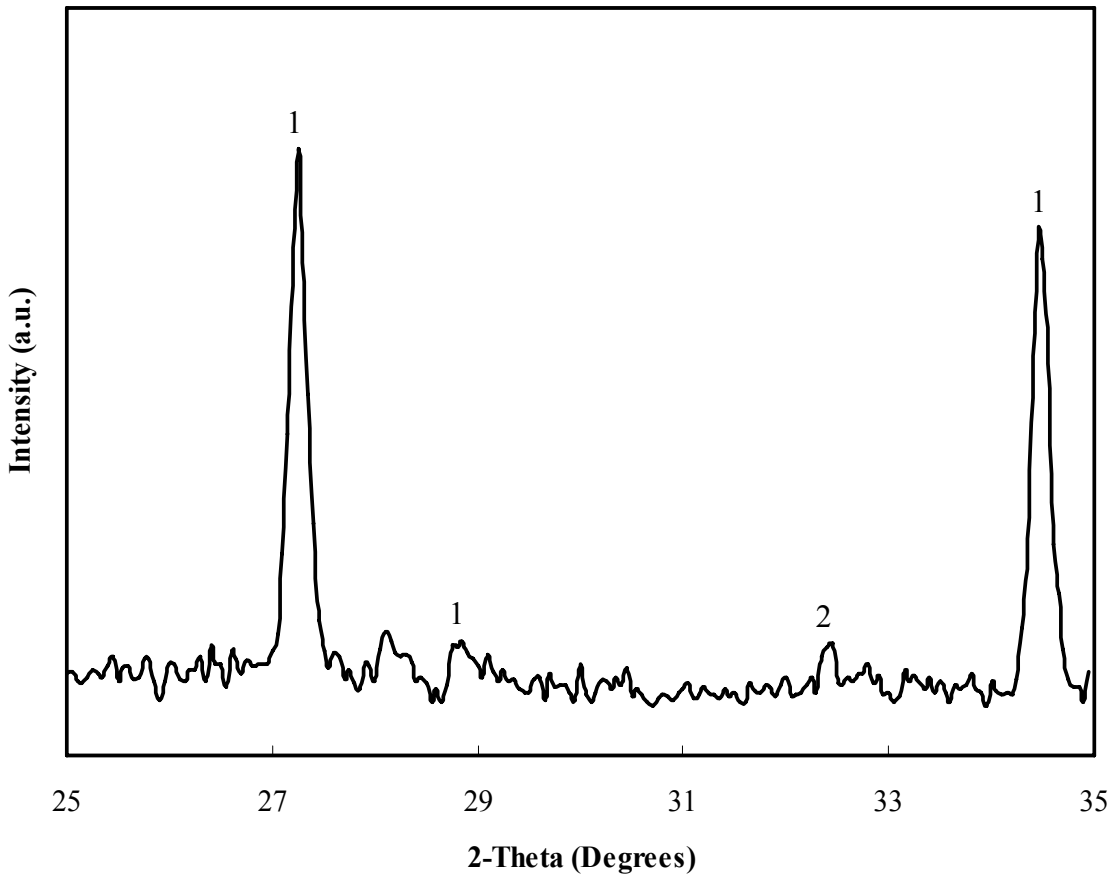

Figure 25. XRD pattern of Al_2O_3- Al_2TiO_5-TiO_2 nanocomposite pellet sintered at 1400°C for 6 h and soaked in SBF for 14 days. The phases are denoted as 1: Al_2TiO_5 and 2: apatite.

XRD plot of the pellet soaked in SBF for 14 days is shown in figure 24. A small peak of apatite was detected.

4.7 Mesurement of Dielectric properties

Electrical properties of the silver paint applied pellet structures were investigated at 1 MHz after heat treatment at 1000°C, 1200°C and 1400°C for 2 h and 6 h to study the effect of phases present, grain size and density. The results are shown in figure 25 (a) and (b).

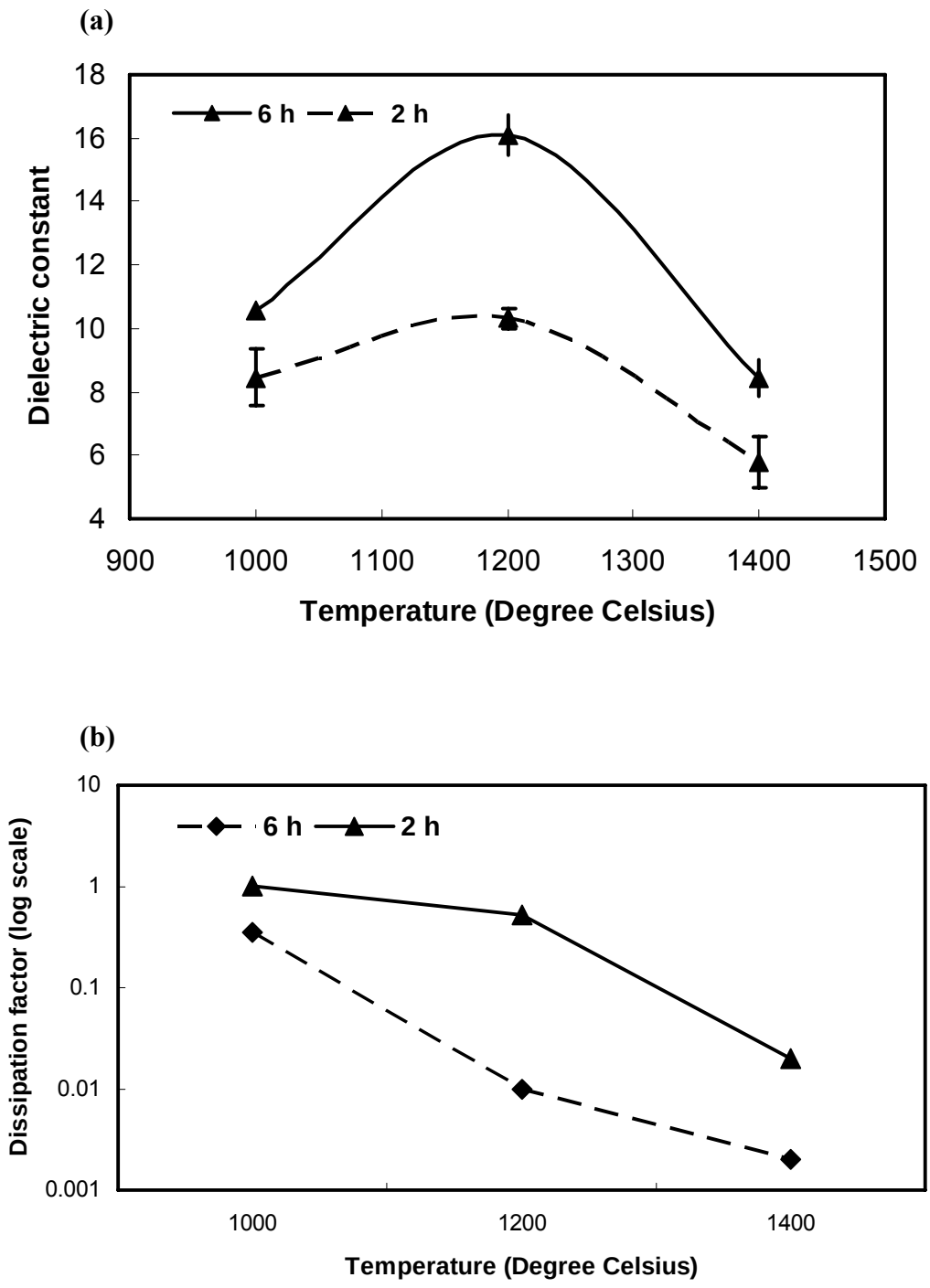

Figure 26. (a) Dielectric constant and (b) dissipation factor of nanocomposite pellet specimens sintered at 1000ºC, 1200ºC and 1400ºC, for 2 h and 6 h respectively.

4.8 Rietveld Refinement of X-Ray Diffraction data

The diffraction patterns obtained after Rietveld refinement are shown in figure 26 (a). The lattice parameter of the refined structure was calculated as a=0.361 nm , b=0.945 nm and c=0.970 nm , background coefficient was fixed as 5, and the grain size factor at 1.1. Figure 16 (b) and (c) are the Rietveld refined plots in a narrow 2-theta range showing the quality of fit.

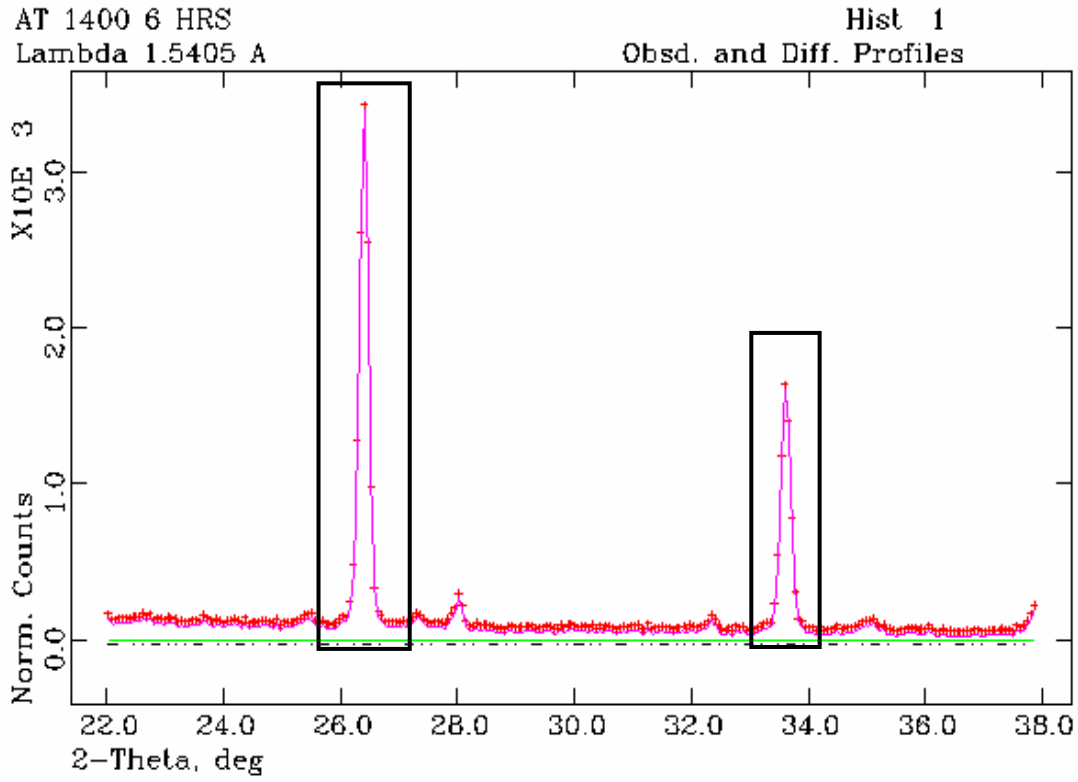

(a)

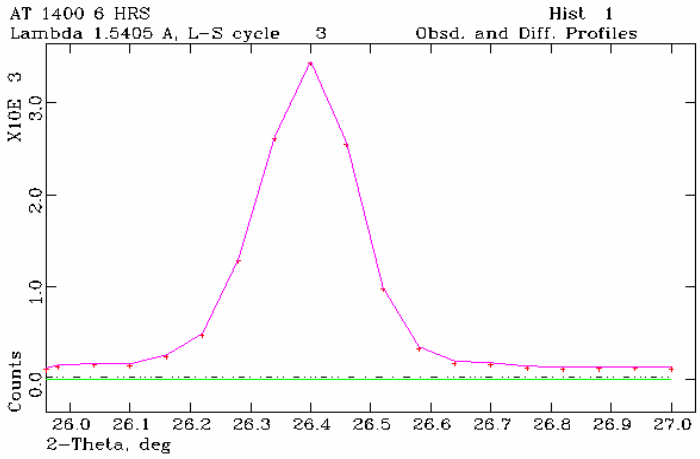

(b)

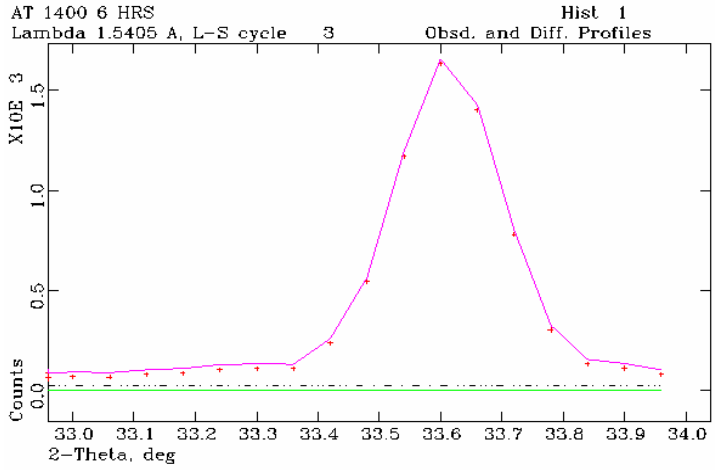

(c)

Figure 27. (a) Rietveld refined plot of the nanocomposite sintered at 1400°C for 6 h in 2-theta range of 22-38°. (b) Rietveld refinement of the plots in a narrow 2θ range of 26-27°. (c) Rietveld refinement of the plots in a narrow 2θ range of 33-34°. It can be seen that almost a perfect fit was obtained confirming high phase purity and orthorhombic crystal structure of aluminum titanate.

CHAPTER FIVE:

DISCUSSION

5.1 Phase evolution and phase transformation in Al_2O_3- Al_2TiO_5-TiO_2 nanocompos*ite*

Sol-gel synthesis can be used to fabricate powder, films, composites or glass and is based on the hydrolysis and condensation of molecular precursors like metal alkoxides or hydroxylated metal ions in aqueous solutions [51]. DSC / TGA analysis (Figure 11) of the as synthesized powder show that heat treatment of the powder should be carried out at temperatures above 400ºC because below this temperature gel contains water and organic constituents. Complete elimination and decomposition of these species occur at temperatures ranging from 100°C to 400°C. The broad plateau at 700ºC on the DSC plot marks the initiation of the powder crystallization which is also confirmed by the XRD plot of the powder (Figure 10). The transformation of as crystallized anatase-TiO_2 and θ-Al_2O_3 into rutile-TiO_2 and α-Al_2O_3 respectively occurs in the temperature range of 800ºC to 1000ºC, indicated by the broad endothermic region. Al_2O_3 generally follows a polymorphic transformation path of γ → δ→ θ→ α [41] and TiO_2 transforms from anatase → rutile phase with increasing temperature. It is generally observed that synthesis of alumina from aluminum alkoxides lead to formation of γ phase at low temperatures which then follows the discussed path on heating and finally transforms into α phase at temperatures around 1180ºC [52]. In this study, powder calcined for 700ºC, 2 h show presence of θ-Al_2O_3 phase which transforms completely into α-Al_2O_3 phase at 900ºC (Figure 12). XRD of powder calcined at lower temperatures were amorphous. This shows that θ-Al_2O_3 phase is the first phase to crystallize instead of the γ-Al_2O_3 phase and the α-Al_2O_3 phase forms at

much lower temperatures than generally observed. We attempt to explain this abnormal behavior on the basis of findings in some earlier reports and the effects of nanosize on a system structure.

Effect of doping 2% TiO_2 on $\gamma \rightarrow \alpha$ (Al_2O_3) phase transition shows that the transformation temperature decreases from 1357ºC to 1164ºC. It is known that both $\gamma \rightarrow \alpha$ and $\theta \rightarrow \alpha$ (Al_2O_3) polymorphic phase transformations are nucleation and growth processes and application of pressure during the consolidation of γ-Al_2O_3 leads to a decrease in the thermodynamic energy barrier and kinetic energy barrier thereby resulting in a lower transformation temperature to α phase . It must be noted that small length scales in nanosize systems directly influence the energy band structure and can lead indirectly to changes in the associated atomic structure. Moreover high surface area to volume ratio (S/V) in nanosize materials may have significant implications on the total energy of the system and may lead to stabilization of metastable structures different from normal bulk structures[53]. Indeed it has been observed that, increased surface energy (γ) provides the additional pressure ($\Delta p = 2 \gamma / r$, r is the particle radius) stabilizing the monoclinic phase in yttria systems rather than coarse grained cubic structure [45]. The average grain size of powder calcined at 900ºC, 2 h as determined by HR-TEM analysis in this study was 12 nm (Figure 13). Assuming that the powder particles calcined at 700ºC, 2 h are even smaller in size it seems that a combination of the presence of TiO_2 and nanoscale effects result in direct formation of θ rather than γ-phase and a low temperature transformation into α-Al_2O_3. Nanoparticles of anatase-TiO_2 particles also show a lower transformation temperature into rutile-TiO_2 phase. Both anatase and rutile-TiO_2 phases are present in 700ºC, 2 h calcined powder (Figure 10) as against a generally observed transformation temperature of higher than 900ºC. The formation temperature of Al_2TiO_5 is around 1280°C and

it is usually unstable below this temperature decomposing into α-Al_2O_3 and rutile-TiO_2 [32]. A nanocomposite of α-Al_2O_3, rutile-TiO_2 and Al_2TiO_5 is observed for powders heat treated at 1300ºC for 2 h (Table 5). Percentage of Al_2TiO_5 phase increases on increasing the time from 2 h (10%) to 6 h (50%) at 1300ºC and highly pure Al_2TiO_5 is obtained for powder sintered at 1300ºC for 6 h.

5.2 Sintering and Densification of Al_2O_3- Al_2TiO_5-TiO_2 nanocomposite

Densification of nanopowder poses formidable challenges. Powder agglomeration, high reactivity, contamination, grain coarsening and loss of nanofeatures are among the main problems [43]. The green density of compact nanopowder structures play an important role in the final sintered density and, inhomogeneities in the green compact are least desirable. The as-synthesized nanopowder was heat-treated at 400ºC for 2 h and were pressed at 15 MPa uniaxially. Although necessary precautions were taken the green density obtained may be a result of manual mode of the press used and / or instrumental limitations. It is also worth noting that a large fraction of atoms in the nanocrystalline materials reside at grain boundaries [54]. Using a simplified equation,

$$\mathbf{C = 3\,\Delta / d} \qquad \textbf{(}\text{Equation 7}\textbf{)}$$

(Where C is the volume fraction of nanocrystalline materials associated with grain boundaries, Δ is the average grain boundary thickness and d is the average grain boundary diameter) Suryanarayana shows that 30% volume fraction of atoms in a 10 nm grain-size material are associated with grain boundaries. It can be argued that grain boundaries have lower densities than adjoining crystalline grains and hence the overall theoretical density of a nanocrystalline material may be lower than coarse grain counterparts.

The maximum sintered density of pellets obtained is 2.95 g/cm^3 at 1400 ºC, 6 h (Figure 15) which is 80% of the theoretical density of Al_2TiO_5 and a final grain size of 92 nm (Table 5). Better densification of Al_2TiO_5 has been obtained by use of techniques like pressure assisted consolidation methods (grain size lower than 200 nm)[55] and field assisted sintering technique[32] (grain size 0.5-30 μm). This has to be considered with a view that we used conventional uniaxial compaction with a ramp and hold heating process and obtained a much finer grain size (Table 5). Figure 18 is the SEM image of pellet structures sintered at 1300ºC, 6 h. The particles are fine in size and the pore density is high which is obvious from the sintered density values. Pellet structures sintered at 1400ºC and 1500 ºC for 6 h show lower pore density but the particle size increases as temperature is increased. Microcracks are observed in pellets sintered at 1500 ºC for 6 h (Figure 19 b). One of the intrinsic problems with aluminum titanate is that its anisotropic thermal expansion on the three axes leads to high internal stresses and microcracking [32]. MgO and Fe_2O_3 modified Al_2TiO_5 has shown a reduction in microcracking and an increase in thermal stability [56].

5.3 Mechanical properties of sintered Al_2O_3- Al_2TiO_5-TiO_2 nanocomposite pellets

Vickers hardness number of sintered pellets (6 h) decreased with increasing sintering temperature (Table 6). Vickers hardness number decreases from 299 to 134 for specimens sintered 1300°C and 1500°C, 6 h respectively. The decrease in hardness values can be attributed to an increase in the amount of Al_2TiO_5 phase with increase in sintering temperature. The presence of microcracks in 1500°C, 6 h sintered specimens further decreases the hardness. It is generally observed that in Al_2O_3 - TiO_2 composites hardness decreases as the mol fraction of TiO_2 increases[6]. The pellet structures sintered at 1300°C, 6 h had the highest biaxial flexure

strength of 43.2 MPa. Biaxial flexure strength decreased as the percentage of aluminum titanate phase increased with increase in sintering temperature. Figure 22 shows the effect of increasing percentage of aluminum titanate on Vickers hardness and Biaxial Flexure strength. Takahashi *et al*. investigated the mechanical properties of Al_2TiO_5 and feldspar doped Al_2TiO_5 obtained by ball milling of α-Al_2O_3 and rutile-TiO_2 powder[57]. Pellet structures sintered at 1500°C for 2 h had a 3-point flexural strength of 3.5 – 3.8 MPa and a steep increase in flexural strength (24.1-25 MPa) was observed for specimens doped with 2% feldspar. It seems that the nanosize of the Al_2TiO_5 phase results in an increase in biaxial flexure strength than its micron size counterpart.

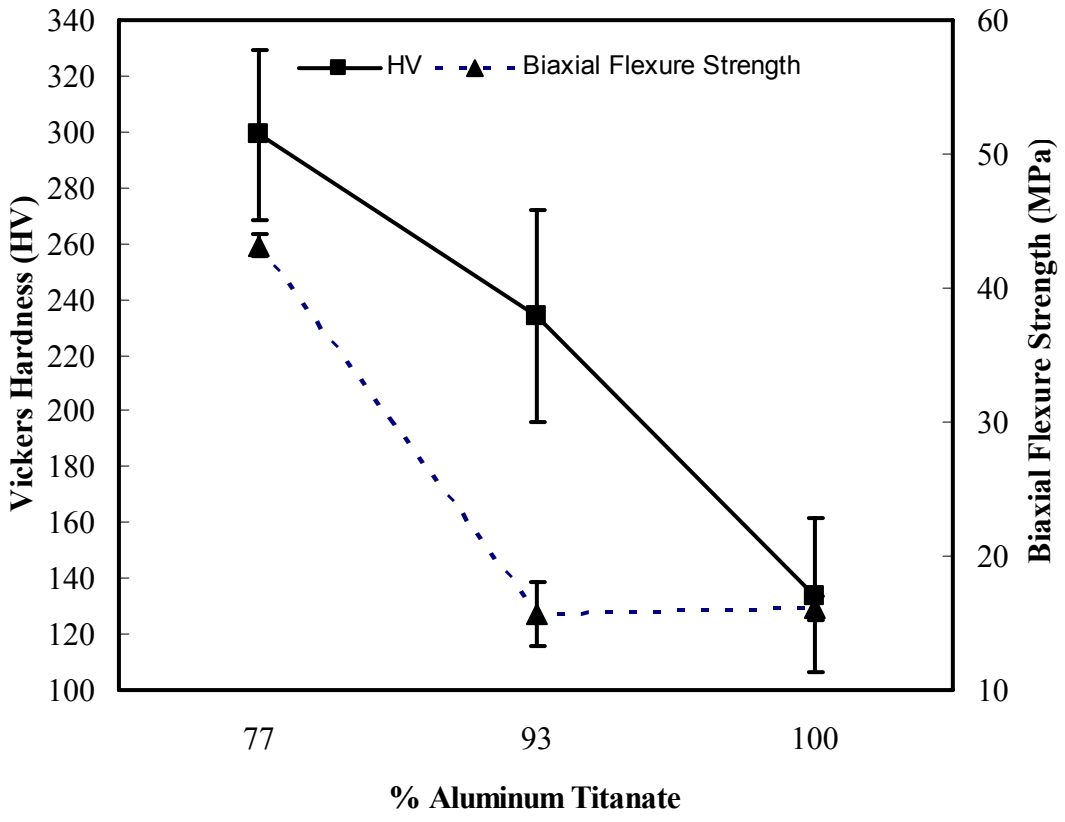

Figure 28. Variation in Vickers hardness number and Biaxial flexure strength of the sintered pellet structures as a function of percentage of Aluminum Titanate present.

5.4 Bioactivity study on sintered Al_2O_3- Al_2TiO_5-TiO_2 nanocomposite pellets

Biocompatibility studies on α-Al_2O_3, rutile-TiO_2 has already been done by a number of researchers and it has been proved that they are biocompatible and apatite growth has been observed on them when soaked in SBF. But there have been no reports of SBF biostudy on Al_2TiO_5. Hence a systematic and detailed study on pellets sintered at 1400ºC, 2 h was carried out. The SEM images shown in figure 21 and 22 and EDX plot shown in figure 24 confirm the growth of apatite crystals / globules on Al_2TiO_5 pellets soaked in SBF after 7 and 14 days respectively. The apatite crystals / globules have mostly circular shape and have a size in the range of 0.5 - 3μm. The number of apatite crystals increase with increasing soaking period. It can be seen that after 14 days of soaking in SBF apatite colonies start to grow on the sintered pellet. XRD of the pellet soaked for 14 days confirms the presence of apatite phase (Figure 23). The pellets after soaking in SBF were dried in furnace at 100°C for 30 min and characterized for Vickers hardness and Biaxial flexure strength for biodegradation study. Both hardness and flexure remained almost constant after soaking in SBF for 7 and 14 days respectively.

Table 7. Change in the Vickers harness and Biaxial flexure strength as a function of soaking time in SBF.

Days soaked in SBF	Vickers hardness (HV)	Biaxial flexure strength (Mpa)
7	261.77	20.26
14	261.23	20.7

5.5 Dielectric properties of sintered Al_2O_3- Al_2TiO_5-TiO_2 nanocomposite pellets

Dielectric constants of the sintered pellet structures have peak values at 1200°C (Figure 26 a) with the highest value of 16.1 for 6 h sintered pellets. Dielectric constants of bulk materials depend on phase composition, defects, density and grain size[58]. The phases present at both 1000°C and 1200°C are crystalline α-Al_2O_3 and rutile-TiO_2 but the pellets have a marked difference of density with the density at 1200°C higher. Even though the density increases at 1400°C the dielectric constant shows a sharp decrease in both cases. This is clearly because of the increased volume fraction of the Al_2TiO_5 phase. It must be pointed out that though pellets sintered for 6 h at 1400°C is pure Al_2TiO_5 their dielectric constant is higher than pellets sintered for 2 h with a composite composition of α-Al_2O_3, rutile-TiO_2 and Al_2TiO_5. This seems to be a result of higher density and the effect of volume expansion due to the phase transformation taking place. The molar volume of α-Al_2O_3, rutile-TiO_2 and Al_2TiO_5 are 25.56, 28.82 and 49.20 cm^3/mol resulting in volume expansion on transformation to Al_2TiO_5.

Considering the pellet as a mixture of α-Al_2O_3 and rutile-TiO_2 the dielectric constant can be calculated using the equation [59],

$$\varepsilon' = [V_m\varepsilon_m (0.66 + \varepsilon_d / 3\varepsilon_m) + V_d\varepsilon_d] / (V_m ((0.66 + \varepsilon_d / 3\varepsilon_m) + V_d)] \quad \text{(Equation 8)}$$

where ε' is the dielectric constant of the mixture, V_m and V_d are the volume fraction of the two phases and ε_m and ε_d are the dielectric constant of the two phases respectively. Taking into consideration the porosity the equation becomes:

$$\varepsilon' = \varepsilon_m [1- \{(3P (\varepsilon_m – 1))/ (2 \varepsilon_m + 1 - P + P\varepsilon_m)\}] \quad \text{(Equation 9)}$$

where, P is the fractional porosity given by P = 1 – D (D is the fractional theoretical density). Taking dielectric constant of α-Al_2O_3 and rutile-TiO_2 as 9 and 80 respectively we first calculate the dielectric constant of a composite with equal volume fraction of both the phases using equation 5. Thereafter using equation 6 and taking dielectric constant of pores as 1 (air), the dielectric constant of the pellets sintered at 1200ºC for 6 h comes out to be 18.1 which compares well with our result of 16.1. The dielectric dissipation factor of a dielectric material is the tangent of the loss angle δ and is used to describe the quality of components. It decreases with increase of sintering temperature and increase in the fraction of Al_2TiO_5 (Figure 26 b). The dissipation factor of pellets is 0.01 at 1200ºC, 6 h.

CHAPTER SIX:

CONCLUSIONS

A detailed systematic study of the sol-gel derived Al_2O_3,-Al_2TiO_5-TiO_2 ceramic nanocomposite was undertaken to establish the correlation between the mechanical, electrical and biocompatibility properties of the nanocomposite to its phase composition and sintering temperature.

a) Sol-gel technique was successfully employed to synthesize nanocomposites of α-Al_2O_3, Al_2TiO_5 and rutile-TiO_2. Almost pure phase Al_2TiO_5 with grain size of 92 nm was obtained on further heating of the nanocomposites to 1400ºC for 6 h.

b) Nanosize of the as synthesized powder results in low temperature phase transformations in Al_2O_3 and TiO_2.

c) Results on densification behavior of pellets show that densification improves with increase in sintering temperature and sintering time. Highest density of 2.95 g/cm^3 is obtained for pellet structures sintered at 1400ºC, 6 h.

d) The nanosize of Al_2TiO_5 phase results in higher biaxial flexure strength than its micron size counterparts. Mechanical properties viz. hardness and biaxial flexure strength decrease with an increase in the percentage of Al_2TiO_5 in the nanocomposite.

e) Bioactivity studies on Al_2TiO_5 were carried out for the first time to the best of our knowledge. SEM images and XRD pattern of the specimens soaked in SBF for 7 and 14 days show the growth of apatite on the nanocomposite specimens. Both the hardness and biaxial flexure strength of the specimen improved after soaking in SBF.

f) Effect of nanosize, porosity and phase evolution on electrical properties has been

discussed. Best combination of dielectric constant ($\kappa = 8.4$) and dissipation factor (0.002) is obtained for pellet structures sintered at 1400ºC for 6 h.

Hence, Al_2O_3,-Al_2TiO_5-TiO_2 ceramic nanocomposite show interesting and promising properties for use as electronic biomaterials. It has a dielectric constant twice as high as silicon dioxide and is biocompatible.

6.1 Future Work / Recommendations

Although the initial results in this study are encouraging a lot needs to be done before aluminum titanate finds the intended applications. The density of pellet structures has a very important effect on the overall behavior like mechanical and dielectric properties. Alternate ways to improve the density of pellet structures can be used to get a much better and clearer idea of the effect of nanosize of grains on these properties. *In vivo* tests on aluminum titanate needs to be done before it can be used either as a structural or bioelectronic materials.

LIST OF REFERENCES

1. Sargeant, A.; Goswami, T., Hip implants: Paper V. Physiological effects. *Materials & Design* 2006, 27, (4), 287-307.
2. Heiduschka, P.; Thanos, S., Implantable bioelectronic interfaces for lost nerve functions. *Progress In Neurobiology* 1998, 55, (5), 433-461.
3. Gopel, W., Bioelectronics and nanotechnologies. *Biosensors & Bioelectronics* 1998, 13, (6), 723-728.
4. Hontsu, S.; Matsumoto, T.; Ishii, J.; Nakamori, M.; Tabata, H.; Kawai, T., Electrical properties of hydroxyapatite thin films grown by pulsed laser deposition. *Thin Solid Films* 1997, 295, (1-2), 214-217.
5. Willner, I.; Willner, B., Biomaterials integrated with electronic elements: en route to bioelectronics. *Trends In Biotechnology* 2001, 19, (6), 222-230.
6. Lee, S. W.; Morillo, C.; Lira-Olivares, J.; Kim, S. H.; Sekino, T.; Niihara, K.; Hockey, B. J., Tribological and microstructural analysis of Al_2O_3/TiO_2 nanocomposites to use in the femoral head of hip replacement. *Wear* 2003, 255, 1040-1044.
7. Piconi, C.; Labanti, M.; Magnani, G.; Caporale, M.; Maccauro, G.; Magliocchetti, G., Analysis of a failed alumina THR ball head. *Biomaterials* 1999, 20, (18), 1637-1646.
8. Willmann, G., Development in medical-grade alumina during the past two decades. *Journal Of Materials Processing Technology* 1996, 56, (1-4), 168-176.
9. Peltola, T.; Jokinen, M.; Rahiala, H.; Patsi, M.; Heikkila, J.; Kangasniemi, I.; Yli-Urpo, A., Effect of aging time of sol on structure and in vitro calcium phosphate formation of sol-gel-derived titania films. *Journal Of Biomedical Materials Research* 2000, 51, (2), 200-208.
10. Hench, L. L., Biomaterials: a forecast for the future. *Biomaterials* 1998, 19, (16), 1419-1423.

11. Editor, Discussion. *Acta Ortho Scan* 2005, 74.

12. S H. Park, A. L., V. K. Goel and J. C. Keller, *Biomaterials principles and applications*. CRC Press: 2003.

13. Cluett, J. Hip Replacement Impant options.

14. Editor, The best hip. *Harvard health letter* 2005, 30, (8), 5.

15. Simoes, J. A.; Marques, A. T., Design of a composite hip femoral prosthesis. *Materials & Design* 2005, 26, (5), 391-401.

16. Kumar, K. S.; Van Swygenhoven, H.; Suresh, S., Mechanical behavior of nanocrystalline metals and alloys. *Acta Materialia* 2003, 51, (19), 5743-5774.

17. Murugan, R.; Ramakrishna, S., Development of nanocomposites for bone grafting. *Composites Science And Technology* 2005, 65, (15-16), 2385-2406.

18. Evans, S. L.; Gregson, P. J., Composite technology in load-bearing orthopaedic implants. *Biomaterials* 1998, 19, (15), 1329-1342.

19. Hench, L. L., The challenge of orthopaedic materials. *Current Orthopaedics* 2000, 14, (1), 7-15.

20. Jamuna Selvakumaran, M. P. H., Member, EEE, David J. Ewins and Peter R. Richards, BIOCOMPATIBILITY STUDIES OF MATERIALS USED FOR CHRONICALLY IMPLANTABLE MICROELECTRODES. *IEEE* 2000.

21. Grayson, A. C. R.; Shawgo, R. S.; Johnson, A. M.; Flynn, N. T.; Li, Y. W.; Cima, M. J.; Langer, R., A BioMEMS review: MEMS technology for physiologically integrated devices. *Proceedings Of The Ieee* 2004, 92, (1), 6-21.

22. Stangel, K.; Kolnsberg, S.; Hammerschmidt, D.; Hosticka, B. J.; Trieu, H. K.; Mokwa, W., A programmable intraocular CMOS pressure sensor system implant. *Ieee Journal Of Solid-State Circuits* 2001, 36, (7), 1094-1100.

23. Kotzar, G.; Freas, M.; Abel, P.; Fleischman, A.; Roy, S.; Zorman, C.; Moran, J. M.; Melzak, J., Evaluation of MEMS materials of construction for implantable medical devices. *Biomaterials* 2002, 23, (13), 2737-2750.

24. Voskerician, G.; Shive, M. S.; Shawgo, R. S.; von Recum, H.; Anderson, J. M.; Cima, M. J.; Langer, R., Biocompatibility and biofouling of MEMS drug delivery devices. *Biomaterials* 2003, 24, (11), 1959-1967.

25. Kingery, W. D., *Introduction to ceramics*. John Wiley and Sons: New York, 1976.

26. Black, J., *Biological performance of matrerials*. Marcel Dekker: New York, 1992; Vol. 2nd.

27. Shamala, K. S.; Murthy, L. C. S.; Rao, K. N., Studies on optical and dielectric properties of Al2O3 thin films prepared by electron beam evaporation and spray pyrolysis method. *Materials Science And Engineering B-Solid State Materials For Advanced Technology* 2004, 106, (3), 269-274.

28. Turunen, E.; Varis, T.; Hannula, S. P.; Vaidya, A.; Kulkarni, A.; Gutleber, J.; Sampath, S.; Herman, H., On the role of particle state and deposition procedure on mechanical, tribological and dielectric response of high velocity oxy-fuel sprayed alumina coatings. *Materials Science And Engineering A-Structural Materials Properties Microstructure And Processing* 2006, 415, (1-2), 1-11.

29. Katiyar, P.; Jin, C.; Narayan, R. J., Electrical properties of amorphous aluminum oxide thin films. *Acta Materialia* 2005, 53, (9), 2617-2622.

30. Hu, Y.; Tsai, H. L.; Huang, C. L., Phase transformation of precipitated TiO2 nanoparticles. *Materials Science And Engineering A-Structural Materials Properties Microstructure And Processing* 2003, 344, (1-2), 209-214.

31. Kaneko, H.; Uchida, M.; Kim, H. M.; Kokubo, T.; Nakamura, T., Process of apatite formation

induced by anatase on titanium metal in simulated body fluid. In *Bioceramics 14*, 2002; Vol. 218-2, pp 649-652.

32. Stanciu, L.; Groza, J. R.; Stoica, L.; Plapcianu, C., Influence of powder precursors on reaction sintering of Al2TiO5. *Scripta Materialia* 2004, 50, (9), 1259-1262.

33. Freudenberg, B.; Mocellin, A., Aluminum Titanate Formation By Solid-State Reaction Of Fine Al2o3 And Tio2 Powders. *Journal Of The American Ceramic Society* 1987, 70, (1), 33-38.

34. Bersuker, G.; Barnett, J.; Moumen, N.; Foran, B.; Young, C. D.; Lysaght, P.; Peterson, J.; Lee, B. H.; Zeitzoff, P. M.; Huff, H. R., Interfacial layer-induced mobility degradation in high-k transistors. *Japanese Journal Of Applied Physics Part 1-Regular Papers Short Notes & Review Papers* 2004, 43, (11B), 7899-7902.

35. Lucovsky, G.; Wu, Y.; Niimi, H.; Misra, V.; Phillips, J. C., Bonding constraints and defect formation at interfaces between crystalline silicon and advanced single layer and composite gate dielectrics. *Applied Physics Letters* 1999, 74, (14), 2005-2007.

36. Gleiter, H., Nanostructured materials: Basic concepts and microstructure. *Acta Materialia* 2000, 48, (1), 1-29.

37. Setter, N., Electroceramics: looking ahead. *Journal Of The European Ceramic Society* 2001, 21, (10-11), 1279-1293.

38. Tepper, T.; Berger, S., Correlation between microstructure and electrical properties of tungsten-silica nanocomposites. *Nanostructured Materials* 1999, 11, (7), 895-907.

39. Tepper, T.; Berger, S., Correlation between microstructure, particle size, dielectric constant, and electrical resistivity of nano-size amorphous SiO2 powder. *Nanostructured Materials* 1999, 11, (8), 1081-1089.

40. Apte, P.; Suits, B. H.; Siegel, R. W., Hardness measurements of nanophase Al/Al-oxide

consolidated composites. *Nanostructured Materials* 1997, 9, (1-8), 501-504.

41. Li, J. G.; Gao, L. A.; Guo, J. K., Mechanical properties and electrical conductivity of TiN-Al2O3 nanocomposites. *Journal Of The European Ceramic Society* 2003, 23, (1), 69-74.

42. Zhang, L. D.; Mo, C. M.; Cai, W. L.; Chen, G., Characterizations of optical absorption in porous Al2O3-Cr2O3 nanocomposites. *Nanostructured Materials* 1997, 9, (1-8), 563-566.

43. Koch, C. C., *Nanostructured materials Proceesing, properties and applications*. William Andrew Publishing: New York, 2002.

44. Seal, S.; Baraton, M. I., Toward applications of ceramic nanostructures. *Mrs Bulletin* 2004, 29, (1), 9-12.

45. Groza, J. R., Nanosintering. *Nanostructured Materials* 1999, 12, (5-8), 987-992.

46. Dowding, J. R. G. a. R. J., Nanoparticulate Particle densification. *Nanostructured Materials* 1996, 7, (7), 749-768.

47. Seal, S. S. a. S., *Synthesis, functionalization and surface treatment of nanoparticles*. American Scienific Publishers: California, 2002.

48. Norton, C. S. a. M. G., *X-Ray Diffraction, A practical Approach*. Plenum Press: New York, 1998.

49. Takadama, T. K. a. H., How useful is SBF in predicting in vivo bone bioactivity? *Biomaterials* 2006, (27), 2907-2915.

50. Lekanova, T. L.; Ryabkov, Y. I.; Sevbo, O. A.; Filippov, V. N., Interactions in the Al2TiO5-Ti2O3 system. *Russian Journal Of Applied Chemistry* 2005, 78, (8), 1223-1228.

51. Scherer, C. J. B. a. G. W., *Sol-Gel Science: The Physics and Chemistry of Processing*. Academic Press Inc: San Diego, 1990.

52. Y. K. Park, E. H. T., M. Zubris, R. Tannenbaum, Size-controlled synthesis of alumina

nanoparticles from aluminum alkoxides. *Materials Research Bulletin* 2005, (40), 1506-1512.

53. R. Kelsall, I. H. a. M. G., *Nanoscale Science and Technology*. John Wiley & Sons Ltd.: West Sussex, 2005.

54. Suryanarayana, C.; Koch, C. C., Nanocrystalline materials - Current research and future directions. *Hyperfine Interactions* 2000, 130, (1-4), 5-44.

55. Duan, R. G.; Zhan, G. D.; Kuntz, J. D.; Kear, B. H.; Mukherjee, A. K., Processing and microstructure of high-pressure consolidated ceramic nanocomposites. *Scripta Materialia* 2004, 51, (12), 1135-1139.

56. T. S. Liu, D. S. P., Long term thermal stability and mechanical properties of aluminum titanateat 1000-1200C. *Journal of Materials Science* 1998, (33), 995-1001.

57. Takahashi, M.; Fukuda, M.; Fukuda, M.; Fukuda, H.; Yoko, T., Preparation, structure, and properties of thermally and mechanically improved aluminum titanate ceramics doped with alkali feldspar. *Journal Of The American Ceramic Society* 2002, 85, (12), 3025-3030.

58. Hornebecq, V.; Huber, C.; Maglione, M.; Antonietti, M.; Elissalde, C., Dielectric properties of pure (BaSr)TiO3 and composites with different grain sizes ranging from the nanometer to the micrometer. *Advanced Functional Materials* 2004, 14, (9), 899-904.

59. Penn, S. J.; Alford, N. M.; Templeton, A.; Wang, X. R.; Xu, M. S.; Reece, M.; Schrapel, K., Effect of porosity and grain size on the microwave dielectric properties of sintered alumina. *Journal Of The American Ceramic Society* 1997, 80, (7), 1885-1888.